

1 **Stochastic asymmetric repartition of lytic machinery in dividing CD8⁺ T**
2 **cells generates heterogeneous killing behavior**

3

4 Fanny Lafouresse^{1,#*}, Romain Jugele^{1,#}, Sabina Müller¹, Marine Doineau², Valérie
5 Duplan-Eche³, Eric Espinosa¹, Marie-Pierre Puissegur¹, Sébastien Gadat² and Salvatore
6 Valitutti^{1,4}

7

8 ¹INSERM U1037, Centre de Recherche en Cancérologie de Toulouse (CRCT), Université
9 de Toulouse III-Paul Sabatier, 31057 Toulouse, France. Team: Molecular dynamics of
10 lymphocyte interaction, « Equipe labellisée Ligue Nationale contre le Cancer 2018 »

11 ²Mathematics of decision making and statistics, Toulouse School of Economics, UMR
12 5604, Université Toulouse 1 Capitole, France

13 ³INSERM, UMR1043, Centre de Physiopathologie de Toulouse Purpan, 31024 Toulouse,
14 France

15 ⁴Department of Pathology, Institut Universitaire du Cancer-Oncopole de Toulouse, 31059
16 Toulouse, France.

17 # These authors contributed equally to this work

18 *Corresponding author: fanny.lafouresse@inserm.fr

19

20

21

22

23

24 **Abstract**

25 Cytotoxic immune cells are endowed with a high degree of heterogeneity in their lytic
26 function, but how this heterogeneity is generated is still an open question. We therefore
27 investigated if human CD8⁺ T cells could segregate their lytic components during
28 telophase, using imaging flow cytometry, confocal microscopy and live cell imaging. We
29 show that CD107a⁺-intracellular vesicles, perforin and granzyme B unevenly segregate in
30 a constant fraction of telophasic cells during each division round. Mathematical modeling
31 posits that unequal lytic molecule inheritance by daughter cells results from the random
32 distribution of lytic granules on the two sides of the cleavage furrow. Finally, we
33 establish that the level of lytic compartment in individual CTL dictates CTL killing
34 capacity.

35 Together, our results show the stochastic asymmetric distribution of effector molecules in
36 dividing CD8⁺ T cells. They propose uneven mitotic repartition of pre-packaged lytic
37 components as a mechanism generating non-hereditary functional heterogeneity in CTL.

38

39 **Key words:** human lymphocytes; Cytotoxic T lymphocytes (CTL); lytic granules; cell
40 division; immunological synapse; lysosomal-associated membrane proteins

41

42

43

44

45

46

47

48

49 **Introduction**

50 Heterogeneity and plasticity of lymphocyte function are key components of successful
51 adaptive immune responses. Accordingly, several studies put forth the notion that
52 individual mouse and human lymphocytes exhibit high degrees of heterogeneity in both
53 their phenotypic and functional characteristics (Beuneu et al., 2010; Buchholz et al.,
54 2016, 2013; Ganesan et al., 2017; Kumar et al., 2018; Lemaitre et al., 2013; Newell et al.,
55 2012). Functional heterogeneity is not limited to cell differentiation and acquisition of
56 phenotypic and functional characteristics, but also involves late steps of immune cell
57 responses such as CD8⁺ cytotoxic T lymphocyte (CTL)- and natural killer (NK) cell-
58 mediated cytotoxicity (Guldevall et al., 2016; Halle et al., 2016). Accordingly, we have
59 previously shown that human CTL belonging to the same clonal population exhibit
60 heterogeneity in their lytic function during sustained interaction with target cells
61 (Vasconcelos et al., 2015). While, some CTL kill a limited number of target cells, others
62 emerge as super-killer cells.

63 One proposed mechanism of functional heterogeneity generation in T lymphocytes is
64 asymmetric cell division (ACD). ACD is a key mechanism to generate cell heterogeneity
65 in biology. It plays a crucial role in embryogenesis by allowing the formation of two
66 distinct cells from a single mother cell (Dewey et al., 2015; Knoblich, 2008). In
67 immunology, ACD has been proposed as a process allowing mouse naive T lymphocytes
68 to divide into short-lived effector T cells and memory T cells, after TCR-triggered
69 division (Arsenio et al., 2015, 2014; Chang et al., 2011, 2007).

70 In the present work, we investigated the possibility that, in dividing human CD8⁺ T cells,
71 heterogeneous distribution of molecules relevant for cytotoxic function into nascent
72 daughter cells might contribute to CTL killing heterogeneity.

73 To address this question, we employed imaging flow cytometry, 3D confocal laser
74 scanning microscopy, live-cell imaging and mathematical modeling to investigate
75 whether and how lytic components might differently segregate in telophase.

76 Our results show that both freshly isolated human peripheral blood CD8⁺ T cells and
77 clonal CTL exhibit a heterogeneous repartition of lytic machinery in telophase during
78 TCR-triggered proliferation which is not part of a classical ACD process. Furthermore,
79 we demonstrate that heterogeneous lytic compartment repartition resets at each round of
80 CTL division and is consequently stationary but not hereditary. Finally, we show that the
81 level of lytic granule expression in individual CTL influences their killing ability.

82 Together, our results unveil a mechanism of stochastic uneven repartition of pre-
83 packaged lytic components within intracellular vesicles that generates functional
84 plasticity during division and contributes to lytic function heterogeneity of individual
85 cells belonging to clonal populations.

86

87

88

89

90

91

92

93

94

95

96 **Results**

97 *Imaging flow cytometry reveals uneven repartition of lytic machinery in dividing human*

98 *CD8⁺ T cells*

99 To investigate the mechanisms leading to the generation of CTL exhibiting
100 heterogeneous killing ability, we first measured the distribution of lytic machinery
101 components in dividing human CD8⁺ T cells. Telophase is the *bona fide* cell cycle phase
102 where unambiguous measurement of molecular repartition in nascent daughter cells is
103 performed (Chang et al., 2007; Filby et al., 2011). Lytic granule repartition during human
104 CD8⁺ T cell division was evaluated using imaging flow cytometry, a technique that
105 combines the advantages of both flow cytometry and microscopy (Basiji and O’Gorman,
106 2015; Doan et al., 2018; Hritzo et al., 2018). This approach allowed us to collect and
107 analyze a substantial number of cells and to visualize and assess the repartition of
108 molecules of interest within individual cells that were unambiguously identified as being
109 in telophase. Cells in telophase were identified using a computer-assisted gating strategy,
110 on the basis of nuclear and tubulin stainings (**Figure 1-figure supplement 1**). Nuclear
111 staining with SYTOXorange[®] identified bi-nucleated cells with elongated shape
112 corresponding to cells in the late steps of division (anaphase and telophase). The cells in
113 telophase were identified (and discriminated from possible cellular doublets) on the basis
114 of tubulin staining that allowed us to highlight their midbodies. **Figure 1-figure**
115 **supplement 2A** shows how masks were applied to delimit the cells and measure the

116 fluorescence intensity of markers of interest in the nascent daughter cells. Cells were also
117 stained with Cell Trace Violet® (CTV), a probe that labels total cell proteins. As
118 previously reported (Filby et al., 2011), we observed that total proteins distribute in
119 nascent daughter cells within a range of 40-60% (**Figure 1-figure supplement 2B**). In
120 our study, CTV staining served both as a marker of cell division (allowing us to identify
121 cells in the different division rounds (Quah and Parish, 2012)), and to define total protein
122 repartition in telophase (Filby et al., 2011). This procedure minimized the possibility that,
123 if some images were taken slightly on an angle, with one daughter cell slightly more in
124 focus than the other, the markers of interest would artificially appear as asymmetric.
125 Indeed, asymmetric distribution was defined as cells in telophase in which repartition of
126 the marker of interest in the nascent daughter cells was beyond the 40-60 % limits
127 observed for CTV repartition (**Figure 1-figure supplement 2B**). In addition, to further
128 exclude the possibility of measurement artifacts, we verified individual cells by eyes and
129 included in the analysis only cells in telophase that were on a even plane. Specificity of
130 staining for the various markers was validated (see Material and Methods section).

131 In a first approach, CD8⁺ T cells freshly isolated from healthy donor blood samples were
132 stimulated with immobilized anti-CD3/anti-CD28/ICAM-1 for 72 hours. Anti-CD3/anti-
133 CD28/ICAM-1 stimulation resulted in activation of human CD8⁺ T cells as shown by cell
134 proliferation and CD137 up-regulation (**Figure 1-figure supplement 3**). Repartition of
135 the lysosomal marker CD107a was investigated in cells in telophase. As shown in **Figure**
136 **1A**, while CTV distribution ranged between 40-60% in dividing T cells, 23 % of
137 telophasic CD8⁺ T cells exhibited an uneven distribution of CD107a⁺ vesicles
138 overcoming the 40-60% CTV range.

139 We next investigated the distribution in telophase of lytic components such as perforin
140 and granzyme B (GrzB), molecules known to be pre-stored in lytic granules. As shown in
141 **Figure 1B** and **C**, perforin and GrzB also unevenly segregated into the two nascent
142 daughter cells in telophase, indicating that daughter cells received a heterogeneous
143 quantity of lytic components.

144 The slope of the linear regression curve for the distribution of CD107a, perforin and
145 GrzB as compared to CTV was close to 0.1, indicating that these 3 molecules distributed
146 independently from total proteins.

147 To define whether uneven repartition of lytic components could be observed in fully
148 differentiated cells, such as memory cells, we investigated CD107a and perforin
149 distribution in telophase in purified human memory CD8⁺ T cells. This analysis showed
150 that also memory CD8⁺ T cells exhibited uneven repartition of CD107a and perforin in
151 telophase (**Figure 1-figure supplement 4**).

152 We next investigated whether lytic machinery asymmetric repartition could also be
153 observed in activated CD8⁺ T cell populations composed of monoclonal cells such as
154 antigen-specific CTL clones. To address this question, we investigated CD107a
155 repartition in CTL undergoing cell division. For this study, we activated CTL clones
156 using immobilized anti-CD3/anti-CD28/ICAM-1 for 72 hours. We opted for this
157 stimulation condition since, in preparatory experiments, we observed that conjugation of
158 CTL with cognate target cells, results (during the 72 hours culture) in the creation of
159 cellular clumps and debris due to CTL killing activity, thus making it difficult and
160 potentially misleading to analyze cells by image flow cytometry and conventional
161 microscopy. As shown in **Figure 1D**, we observed that in clonal CTL undergoing cell

162 division, 15% of the two nascent daughter cells in telophase exhibited uneven distribution
163 of CD107a, thus confirming and extending observations obtained using CD8⁺ peripheral
164 blood T cells.

165 Taken together, the above results indicate that a lysosomal-associated membrane protein
166 known to be a marker of lytic granules and effector molecules involved in CTL lytic
167 function, unevenly segregate in 10-23 % of individual human CD8⁺ T cells undergoing
168 division.

169

170 *Confocal laser scanning microscopy confirms uneven repartition of lytic machinery in*
171 *dividing CD8⁺ T cells*

172 Image flow cytometry allows the unambiguously identification and capture of rare events
173 within a cell population, such as cells in telophase, albeit exhibiting a lower resolution
174 when compared to classical imaging methods. This notion prompted us to confirm results
175 obtained using imaging flow cytometry, with additional methods.

176 We therefore used 3D confocal laser scanning microscopy to measure CD107a content in
177 telophasic CD8⁺ T cells following stimulation with immobilized anti-CD3/anti-
178 CD28/ICAM-1. Although this approach allowed us to collect a relatively small number
179 of cells in telophase (n=61 compared to n=908 obtained by image flow cytometry), it
180 revealed that 27% of the CD8⁺ T cells in telophase exhibited uneven repartition of
181 CD107a, above a 1.5 threshold (corresponding to the 40-60% range used in imaging flow
182 cytometry experiments) (**Figure 2A**). **Figure 2B** depicts the maximum intensity
183 projection (MIP) of a z-stack of images on which measurements of fluorescence intensity
184 were performed (left panel) and a central z-section (right panel). The asymmetry of

185 CD107a repartition in nascent daughter cells is better appreciated by looking at the 3D
186 reconstructions of the dividing cell (**Video 1**).

187 Together, the above results indicate that confocal laser scanning microscopy provides
188 results that reinforce those we obtained using imaging flow cytometry and supports the
189 finding that lytic granules undergo uneven repartition in ~20% of dividing CD8⁺ T cells.

190

191 *Uneven repartition of lytic machinery is not accompanied by asymmetric segregation of*
192 *fate determining transcription factors and does not require a polarity cue*

193 The observation that lytic components were unevenly inherited in daughter cells
194 prompted us to investigate whether this process was somehow related to mechanisms of
195 cell fate determining ACD, a process reported to play a role in mouse naive T
196 lymphocytes differentiation (Arsenio et al., 2015, 2014; Kaminski et al., 2016; Pham et
197 al., 2014). Indeed, it has been reported that ACD can result in the generation of one
198 daughter cell predisposed to become a short-lived effector cell (harboring a high level of
199 the transcription factors T-bet and c-myc, and of GrzB) and one daughter cell predisposed
200 to become a memory T cell (Widjaja et al., 2017). We investigated whether uneven
201 repartition of fate determining transcription factors T-bet and c-myc (Chang et al., 2011;
202 Verbist et al., 2016), might occur in telophase in freshly isolated peripheral blood CD8⁺
203 T cells stimulated with anti-CD3/anti-CD28/ICAM-1 for 72 hours. As shown in **Figure**
204 **3A** and **B**, both T-bet and c-myc did not unevenly segregate into the two nascent daughter
205 cells during telophase. Moreover, the slope of the linear regression curve for the
206 distribution of T-bet and c-myc as compared to CTV was close to 1, indicating that the
207 repartition of these 2 molecules in telophase followed that of total proteins.

208 To further define whether the observed uneven repartition of lytic components was or
209 was not related to ACD, we investigated whether uneven repartition of lytic components
210 was dependent on a polarity cue (e.g. localized TCR stimulation) as previously described
211 for ACD (Arsenio et al., 2015; Pham et al., 2014). **Figure 4A** and **B** shows that a polarity
212 cue was not required to induce uneven distribution of lytic molecules, since comparable
213 CD107a⁺ vesicles segregation was observed in peripheral blood CD8⁺ T cells stimulated
214 by either immobilized (anti-CD3/anti-CD28/ICAM-1) or soluble (PMA + ionomycin)
215 stimuli.

216 Overall, the above results demonstrate that uneven partitioning of lytic compartment in
217 telophase is not associated with asymmetric segregation of fate determining transcription
218 factors. Moreover, a polarity cue is not required. All in all, the above results show that,
219 in human CD8⁺ T cells, lytic machinery uneven repartition is not related to described
220 mechanisms of fate determining ACD.

221

222 *Asymmetric repartition of CD107a⁺ vesicles reset at each division event and generates*
223 *heterogeneous daughter cells*

224 We next investigated whether lytic machinery uneven repartition occurred during
225 subsequent divisions and whether this process could be involved in preserving lytic
226 machinery heterogeneity within CD8⁺ T cell populations.

227 We considered the cells in the different rounds of division (identified by different peaks
228 of CTV dilution, **Figure 1-figure supplement 3**) and analyzed CD107a repartition in
229 telophasic cells. This analysis showed that, in all division rounds considered, a

230 comparable percentage of cells underwent heterogeneous repartition of CD107a (**Figure**
231 **5A and B**).

232 A complementary observation indicated that the heterogeneity process is stationary but
233 not hereditary: e.g. a daughter cell originating from a heterogeneous division has a
234 constant stationary probability to produce a new uneven division. We arrived to this
235 conclusion by generating CD107a fluorescence intensity (CD107a-FI) density curves of
236 all telophasic cells having undergone 0, 1 or 2 mitosis. Cells in telophase showing
237 unequal CD107a-FI repartition were then plotted on these curves (**Figure 5C**). The χ^2
238 statistical test showed that these cells were randomly and independently distributed on the
239 CD107a-FI density curves, supporting the hypothesis that there is no inheritance in the
240 decision to divide unevenly (see Materials and Methods section).

241 We next asked whether this process might create a drift in lytic compartment content in
242 daughter cells leading to the emergence of cellular subsets expressing higher or lower
243 levels of CD107a. To address this question, we analyzed the total CD107a-FI in all G1
244 cells (either undivided or following each division round). As shown in **Figure 5D**, the
245 total CD107a-FI appeared to be broadly similar in the different rounds of division in the
246 whole populations, suggesting that uneven repartition of CD107a, in a relatively constant
247 fraction of cells at each division round, does not lead to the emergence of well-defined
248 cellular subsets expressing higher or lower levels of CD107a. We employed the
249 Kolmogorov-Smirnov goodness of fit test to determine whether the different curves
250 followed the same distribution or not. The test strongly rejected the hypothesis that the
251 CD107a expression curves follow the same distribution during the first two division
252 rounds (see Materials and Methods section), indicating that during these division events

253 randomly heterogeneous populations were generated. Nevertheless, our test also showed
254 that the Kolmogorov distance decreased when the number of divisions increased,
255 indicating that CD107a-FI density distribution seems to be convergent with a higher
256 number of divisions. To define where variability was located in the curves, we employed
257 the χ^2 test. The test showed that variability was distributed all over the curves (i.e. for
258 all the CD107a-FI). Together, Kolmogorov-Smirnov goodness of fit and χ^2 tests revealed
259 a non-stationary variability in the content of CD107a⁺ vesicles in CD8⁺ T cells during
260 early division events.

261 Taken together, the above results indicate that asymmetric distribution of CD107a⁺
262 vesicles in telophase is not limited to the first division, but it is rather a stochastic
263 process, inherent to each division, that perpetuates variability in daughter cells.

264

265 *Lytic granules randomly distribute on the two sides of the cleavage furrow*

266 To gain direct information about the possibility that lytic components might
267 stochastically distribute in nascent daughter cells, we visualized lytic granule repartition
268 during division in individual CTL transfected with mCherry-tagged GrzB mRNA, by live
269 cell microscopy. mCherry-tagged GrzB showed no preferential localization within cell
270 cytosol at the different phases of the division and appeared to randomly partition into the
271 two nascent daughter cells. In some cases, nascent daughter cells exhibited approximately
272 similar repartition of lytic granules (**Figure 6A, Video 2**), in some other cases lytic
273 granule repartition appeared to be rather asymmetric (**Figure 6B, Video 3**). Furthermore,
274 we investigated cell division in 4D (3D plus time). Sorted CD8⁺ T cells in G2/M phase
275 were loaded with LysoTracker Red (LTR) to stain their late endosomal lysosomal

276 vesicles (of which lytic granules are an important fraction (Faroudi et al., 2003)). Nascent
277 daughter cells were imaged to monitor distribution of LTR⁺ vesicles and measure the
278 integrated fluorescence intensity. An example of one CD8⁺ T cell distributing LTR⁺
279 vesicles in a symmetric fashion during division is shown in **Figure 6C** and **Video 4** (LTR
280 distribution ranged within 40-60% at all time points measured). One CD8⁺ T cell that
281 distributed in an asymmetry fashion LTR⁺ vesicles is shown in **Figure 6D** and **Video 5**
282 (LTR distribution ranged above or below 40-60% at all time points measured).
283 Additional examples of cells dividing in symmetric and asymmetric fashion are shown in
284 **Figure 6-figure supplement 1** and **Video 6**.

285 While lytic granules seemed to be overall randomly distributed between nascent daughter
286 cells, in some cases the videos showed that lytic granules did not behave completely
287 independently from each other and exhibited some clustering. We therefore used a
288 computational approach to establish whether the above-described process might be linked
289 to a random repartition of lytic components into the two nascent daughter cells. We first
290 calculated the probability to obtain an asymmetric distribution of lytic granules (*e.g.* a
291 repartition of the granules into the two daughter cells out of the 40-60% range) related to
292 the granule number per dividing cell. This computation is naturally handled with a
293 binomial modeling for the behavior of the population of *n* granules (see Materials and
294 Methods section). This analysis showed that for *n* <100 the probabilities that individual
295 particles distribute asymmetrically on the two sides of the cleavage furrow are relatively
296 high (**Figure 6E**). Using stimulated emission depletion (STED) on CTL stained for GrzB,
297 we estimated that 14 to 65 (mean = 37) lytic granules are contained within individual
298 CTL. Our estimation well-matched with numbers published in previous studies, ranging

299 between 10 and 100 (Chiang et al., 2017; Clark et al., 2003; Kataoka et al., 1996; Peters
300 et al., 1991).

301 These values are compatible with a significant probability of stochastic uneven
302 repartition of lytic granules in telophase, assuming that all lytic granules behave
303 independently.

304 Since our videos indicate that lytic granules might form transitory aggregates within
305 confined intracellular spaces, we upgraded our mathematical simulation of lytic granule
306 repartition in telophase to include the possibility that lytic granules might not segregate
307 completely independently. We simulated particle correlation during cell division for 10 to
308 100 particles. To evaluate the correlation level between individual particles during cell
309 division (ranging from 0 = absence of correlation to 1 = 100% correlation) for a given
310 probability of asymmetric repartition (outside the interval [40%-60%]), we used a Monte-
311 Carlo approach (see Material and Methods section).

312 The analysis shows that for a probability of 20% asymmetric repartition of particles
313 (corresponding to 20% uneven repartition of lytic granules during cell division
314 experimentally measured by imaging flow cytometry and confocal imaging), particle
315 correlation has a relatively low value (4% for 37 particles, 0.04; CI95%, 0.035-0.045),
316 suggesting that lytic granules mainly segregate independently during cell division.

317 Taken together, cell imaging and computational results strongly suggest that the observed
318 stationary unequal distribution of lytic granules in telophase is the result of a stochastic
319 repartition of particulate cytosolic structures on the two sides of the cleavage furrow in
320 dividing cells.

321

322 *The level of lytic granule content in individual CTL dictates CTL killing capacity*

323 To assess the consequences of an uneven distribution of lytic compartment on CTL-

324 mediated cytotoxicity, we investigated cytotoxic efficacy in CTL expressing high and

325 low_lytic granule content. Clonal CTL were loaded with LysoTracker blue, and cells

326 containing high (LysoTracker^{High}) and low (LysoTracker^{Low}) levels were FACS sorted.

327 As shown in **Figure 7A**, sorted LysoTracker^{High} and LysoTracker^{Low} CTL populations

328 maintained their difference in LysoTracker staining at least 24 hours after cell sorting.

329 The cytotoxic efficacy of sorted CTL populations was compared at different

330 effector:target (E:T) ratios by measuring the percentage of killed targets (7-AAD

331 positive targets). For each ratio, LysoTracker^{High} CTL were more efficient than

332 LysoTracker^{Low} CTL in exerting cytotoxicity (**Figure 7B-C**), although basal killing (in

333 the absence of peptide stimulation) was comparable between LysoTracker^{High} and

334 LysoTracker^{Low} CTL (**Figure 7C**). The above results indicated that lytic granule content

335 is associated with killing efficacy. To strengthen these findings, we performed additional

336 experiments on sorted CTL for high and low LysoTracker staining and measured CD107a

337 surface exposure and CD8 internalization following 4 hour conjugation with target cells.

338 Results show that LysoTracker^{high} CTL exhibited a higher lytic granule secretion as

339 detected by CD107a exposure when compared to LysoTracker^{low} CTL (**Figure 7D**).

340 However, productive TCR engagement was comparable in both populations as detected

341 by similar levels of CD8 internalization (Huang et al., 2019; Xiao et al., 2007) (**Figure**

342 **7E**).

343 Together, these results indicate that the lytic granule cargo of individual CTL and not

344 their activation properties directly impact killing behavior. They imply that stochastic

- 345 uneven distribution of lytic granules in dividing CTL determine heterogeneous killing
346 behavior at the single cell level.

347 **Discussion**

348 In the present study we found that, in both freshly isolated peripheral blood CD8⁺ T cells
349 and clonal CTL, ~ 20 percent of telophasic cells undergoes asymmetric distribution of the
350 lytic compartment into the two daughter cells. Our results establish that CD8⁺ killing
351 capacity is associated to lytic compartment level and strongly suggest that uneven lytic
352 machinery repartition produces CD8⁺ T cell populations with heterogeneous killing
353 capacities.

354 We used imaging flow cytometry, a technique that combines the advantages of flow
355 cytometry and microscopy and allows the detection and analysis of rare cells within
356 whole cell populations on the basis of their morphological and staining characteristics
357 (Basiji and O’Gorman, 2015; Doan et al., 2018; Hritzo et al., 2018). We thus acquired
358 and analyzed a significant number of relatively rare events of T cell divisions by
359 precisely identifying cells in telophase. The use of CTV distribution as a parameter of
360 global protein repartition in telophase together with the acquisition of an important
361 number of cell divisions strengthens our analysis. In addition, we investigated lytic
362 granule repartition in dividing CD8⁺ T cells by 3D confocal laser scanning microscopy
363 and 4D live cell imaging. These techniques allowed visualization of lytic granule
364 repartition in telophase with a high time/space resolution and strengthened imaging flow
365 cytometry data by providing unambiguous visualization of lytic granule partitioning.

366 Our results demonstrate that the uneven lytic machinery distribution is not related to
367 ACD.

368 In mouse T lymphocytes, ACD has been reported as a mechanism contributing to the
369 generation of effector/memory daughter cells following division of an individual naive T

370 cell in response to polarizing cues (Arsenio et al., 2015; Chang et al., 2007).
371 Establishment of asymmetry has been associated to the uneven inheritance by daughter
372 cells of transcription factors such as c-Myc and T-bet known for their role in the
373 induction of metabolic reprogramming and in the acquisition of T cell effector function
374 respectively (Chang et al., 2011; Verbist et al., 2016). Following the original observation
375 of uneven repartition of proteasomes in dividing mouse CD4⁺ T cells leading to
376 asymmetric degradation of T-bet in daughter cells (Chang et al., 2011), additional cellular
377 effectors including metabolic and signaling pathways have been found to be implicated in
378 fate determining ACD in mouse naive T lymphocytes (Kaminski et al., 2016; Pollizzi et
379 al., 2016; Verbist et al., 2016). Our results, by showing that lytic granule repartition is not
380 accompanied by a detectable asymmetric segregation of T-bet and c-Myc and does not
381 require a polarity cue, suggest that the lytic machinery uneven distribution observed in
382 human CD8⁺ T cells is not related to previously described ACD. Although we could not
383 detect an asymmetric repartition of classical lineage-determining transcription factor, in
384 our models, this observation does not exclude the possibility that ACD might play a role
385 in the differentiation of human naive T cells into effector and memory subsets during
386 initial antigen specific immune responses. It is therefore possible that the discrepancy
387 between our results and previous studies on ACD in mouse T lymphocytes arises from
388 the different nature of the cells involved in the study. It should also be noted that, beside
389 ACD, other mechanisms can contribute to the generation of different T lymphocyte
390 populations from naive lymphocytes and, more in general, can play a role in T
391 lymphocyte heterogeneity. Alternative models postulate that lymphocyte differentiation
392 might be achieved via the accumulation of progressive differences among daughter cells

393 due to variation in the quantity of the inherited proteins (Buchholz et al., 2016; Cobbold
394 et al., 2018; Gerlach et al., 2013; Girel and Crauste, 2019; Pham et al., 2014; Rohr et al.,
395 2014; Schumacher et al., 2010).

396

397 A puzzling question is how asymmetric distribution of lytic components in telophase is
398 generated. Our results provide a stepping-stone to answer this question. First,
399 mathematical analysis of our imaging flow cytometry data provides an interpretation of
400 our results that is compatible with a stochastic distribution of lytic components during
401 cell division. On one hand, mathematical analysis shows that the process of asymmetric
402 distribution is stationary in terms of the fraction of involved cells: e.g. occurs always on a
403 similar percentage of cells, at each division round, in different experiments and following
404 different stimuli. On the other hand, the heterogeneity process, although stationary is not
405 hereditary: e.g. a daughter cell originating from a heterogeneous division has a constant
406 stationary probability to produce a new uneven division. Second, live-cell imaging shows
407 lytic granule distribution during mitosis. We did not observe any specific pattern of lytic
408 granule repartition (polarization at the membrane or close to the cleavage furrow) before
409 or during cell division. Instead, lytic compartments appeared randomly distributed in cell
410 cytosol. Our observations are consistent with the mathematical modeling of intracellular
411 vesicle distribution showing the high probability of an uneven distribution of a relatively
412 small quantity of granules. In other words, pre-packaged molecular components within a
413 few relatively big vesicles might have higher probability to be asymmetrically partitioned
414 in telophase than molecular components dispersed throughout the cytosol.

415 Moreover, it should be noted, that our videos and results in Figure 6 suggest that, in a

416 limited number of division events, granules might not segregate completely
417 independently from each other, implying that some active mechanism of granule
418 segregation might contribute, to a minor extent, to lytic granule repartition in telophase.
419 Together, our results point out a mechanism of heterogeneity generation that is for the
420 most part stochastic and might be a general mechanism for generating heterogeneity in
421 dividing cells. The possibility that particulate material is unevenly distributed in
422 telophase into two nascent daughter cells has been proposed for other organelles and in
423 other cellular systems (Bergeland et al., 2001; Carlton et al., 2020; Sanghavi et al., 2018).
424 Indeed, in MDCK cells, microscopy analysis and mathematical modelling based on the
425 laws of probability suggested that endosomes/lysosomes partitioning between daughter
426 cells is stochastic (Bergeland et al, 2001). Others show that in telophasic cells, endosomal
427 compartments are clustered at the cleavage furrow, suggesting that microtubules are
428 involved in this process. However, no mechanism ensuring endosomal compartment
429 anchorage to either spindle has been revealed, suggesting that this repartition is
430 stochastic. Similarly, in Dictyostelium cells, it has been demonstrated that dynein and
431 kinesin motors drive phagosomes segregation independently of each other and
432 stochastically (Shanghavi et al 2018). To our knowledge, our present study is the first to
433 relate a mechanism of a random segregation of organelles to functional heterogeneity of
434 immune cells.

435

436 What could be the functional role of asymmetric molecular segregation during mitosis in
437 human CD8⁺ T cells? We propose that a mechanism of asymmetric distribution in
438 telophase (that is stationary at each division, but not inherited by daughter cells) can be

439 instrumental to randomly generate short-lived CTL cohorts harboring functional
440 heterogeneity while ensuring globally reproducible antigen specific CD8⁺ T cell
441 responses. This process might confer robustness to CTL responses through population
442 averaging (Buchholz et al., 2016; Hodgkin et al., 2014).

443

444 It is interesting to note that our results present analogies with previously published data in
445 which asymmetric segregation of internalized exogenous antigen was found to occur
446 during B cell division (Thaunat et al., 2012). Together with this previous study, our
447 results reveal an intriguing capacity of both T and B cells to stochastically distribute in
448 telophase their acidic compartments: MHC Class II compartments for B cells and lytic
449 granules for CD8⁺ T cells. Thus, stochastic distribution in telophase appears to be a major
450 mechanism ensuring a high variability of both humoral and cellular adaptive immune
451 responses during lymphocyte clonal expansion.

452

453

454

455

456

457

458

459

460

461

462

463

464 **Material and Methods**

465

466 **Key resources table**

Reagent type (species) or resource	Designation	Source or reference	Identifiers	Additional information
cell line (<i>Homo-sapiens</i>)	HLA-A2 restricted CD8+ T cell clone (VLAELVKQI)	(Khazen et al., 2016)		
cell line (<i>Homo-sapiens</i>)	HLA-A2 restricted CD8+ T cell clone (NLVPMVATV)	(Khazen et al., 2016)		
cell line (<i>Homo-sapiens</i>)	HLA-A2 restricted CD8+ T cell clone (VLAELVKQI)	(Khazen et al., 2016)		
cell line (<i>Homo-sapiens</i>)	JY (EBV-transformed B cells)	(Khazen et al., 2016; Vasconcelos et al., 2015)		
biological sample (<i>Homo-sapiens</i>)	Buffy coats of Healthy donors	EFS, Toulouse, France		with consent and approval AC-2014-2384
antibody	Anti-human CD3 (Human monoclonal, TR66)	Enzo	cat# ALX-804-822 RRID:AB_2051037	(1 µg/ml)
antibody	Anti-human CD28 (Mouse monoclonal, CD28.2)	eBioscience	cat# 16-0289-81 RRID:AB_468926	(1 µg/ml)
recombinant protein	Recombinant human ICAM-1-Fc fusion protein	R&D Systems	cat# 720-IC	(0.5µg/ml)

antibody	Anti-human CD107a (Mouse monoclonal, H4A3)	BD Pharmingen	cat# 555798 RRID:AB_3 96132	(10µg/ml)
antibody	Anti-human CD107a AlexaFluor® 647 (Mouse monoclonal, H4A3)	BD Pharmingen	cat# 562622 RRID:AB_273 7684	(diluted at 1/100)
antibody	Anti-human Granzyme B (Mouse monoclonal, GB11)	Thermo Scientific	cat# MA1- 80734 RRID:AB_9 31084	(10µg/ml)
antibody	Anti-human Granzyme B AlexaFluor® 647 (Mouse monoclonal, GB11)	BD Pharmingen	cat# 561999 RRID:AB_1 0897997	(10µg/ml)
antibody	Anti-human T-bet (Rabbit polyclonal, Tbx21)	Abcam	cat# ab181400	(10µg/ml)
antibody	Anti-human C-myc (Mouse monoclonal, 9E10)	Thermo Scientific	cat# MA1- 980 RRID:AB_558 470	(10µg/ml)
antibody	anti-human α-tubulin (Rabbit polyclonal)	Abcam	cat# ab15246 RRID:AB_3 01787	(diluted at 1/100)
antibody	anti-mouse IgG1 Alexa Fluor 647 (Goat polyclonal)	Invitrogen	cat# A21240 RRID:AB_2 535809	(10µg/ml)
antibody	anti-mouse IgG1 Alexa Fluor 488 (Goat polyclonal)	Invitrogen	Cat # A- 21121 RRID:AB_2 535764	(10µg/ml)
antibody	anti-rabbit (H+L) AlexaFluor® 488 (Goat polyclonal)	Invitrogen	cat# A11034 RRID:AB_2 576217	(10µg/ml)

antibody	anti-rabbit (H+L) AlexaFluor® 647 (Donkey polyclonal)	Invitrogen	cat# A31573 RRID:AB_2 536183	(10µg/ml)
antibody	anti-rabbit AlexaFluor® 555 (Goat polyclonal)	Invitrogen	cat# A21428 RRID:AB_2 535849	(10µg/ml)
antibody	anti-mouse IgG Abberior Star 580 (Goat polyclonal)	Abberior Instruments	cat# 52403	(10µg/ml)
antibody	Anti-human CD107a- PEcy7 (mouse monoclonal, H4A3)	BD Pharmingen	cat# 561348 RRID:AB_1 0644018	(diluted at 1/50)
antibody	Anti-human CD8- FITC (mouse monoclonal, HIT8A)	BD Pharmingen	cat# 555634 RRID:AB_3 95996	(diluted at 1/50)
recombinant DNA reagent	MGC Human GZMB Sequence verified cDNA (Clone Id: 5223876)	GE Healthcare BIO Sciences	cat# MHS6278- 202801737	
recombinant DNA reagent	mCherry-SEpHluorin	(Koivusalo et al., 2010)	Addgene cat# 32001	
recombinant DNA reagent	pT7-GZMB- mCherry-SEpHluorin	This paper		
sequence-based reagent	Primer : XhoI-T7-GzB Forward caaCTCGAGTAATAC GACTC ACTATAGGGAGACC CGGTA CCatgcaaccaatcctgcttct gcc	This paper		
sequence-based reagent	Primer: EcoRI-GzB- noSTOP-R caaGAATTCgggcgtg gcgttcatggtttctttatcc ag	This paper		

peptide, recombinant protein	CMV peptide p65 (NV-9)	GeneCust	cat# 181329	
peptide, recombinant protein	Human rIL-2	Miltenyi Biotec	cat# 130- 097-748	(150 IU/ml)
peptide, recombinant protein	Human rIL-15	Miltenyi Biotec	cat# 130- 095-766	(50ng/mL)
commercial assay or kit	EasySep Negative human CD8+ T cell isolation kit	StemCell Technologies	cat# 17953	
commercial assay or kit	EasySep human Memory CD8+ T cell enrichment kit	StemCell Technologies	cat# 19159	
software, algorithm	IDEAS SpotCount Threshold (M03,nucleus,60)	Amnis, Luminex		
software, algorithm	IDEAS Area Range Threshold (M02,tubulin,75), 50- 5000, 0-0.5	Amnis, Luminex		
software, algorithm	Fiji	(Schindelin et al., 2012)		
software, algorithm	Imaris Software	Oxford Instruments		
software, algorithm	ZEN ZEISS Efficient Navigation			
software, algorithm	Huygens Professional version 18.10 using CMLE algorithm with SNR:7	Scientific Volume Imaging, USA		STED images were deconvolved

software, algorithm	Python software version 3.5			χ^2 of independence test, χ^2 of homogeneity test and Kolmogorov- Smirnov goodness of fit test
software, algorithm	GraphPad Prism software version 5 for windows			Paired Student's t-test
software, algorithm	FlowJo software	TreeStar		
other	SYTOX™ Orange Dead Cell Stain	Thermo Fisher Scientific	cat# S11368	Manufacturer recommended dilution
other	DAPI	Molecular Probes, Invitrogen™	cat# D1306 RRID:AB_26 29482	
other	Hoechst 33342	ThermoFisher Scientific	cat# 1399	(200 ng/ml)
other	CellTrace™ Violet Cell Proliferation kit	ThermoFisher Scientific	cat# C34557	(5 μ M)
other	LysoTraker Blue (DND22) Dye	Molecular probes	cat# L7525	(200 nM)
other	LysoTraker Red (DND99) Dye	Molecular probes	cat#L7528	(200 nM)
other	7-Aminoactinomycin D (7-AAD)	BD Pharmingen™	cat# 559925	(0.25 μ g)
other	Ibidi μ -slide chambered coverslips Angiogenesis	Ibidi, Biovalley	cat# 81506	
other	Ibidi μ -slide chambered coverslips 8 well	Ibidi, Biovalley	cat# 80821	

other	Nunc Lab-Tek chamber slides 8 wells	Nunc, ThermoFisher	cat#1 54526	
other	Micromesh array (100µm)	Microsurface, Tebu- Bio	cat# MMA-0500-100-08-01	

467

468 ***Experimental model and subject details***

469 Peripheral blood mononuclear cells were isolated from buffy coats of healthy donors
470 obtained through the Etablissement Français du Sang (EFS, Toulouse, France). Blood
471 samples were collected and processed following standard ethical procedures (Helsinki
472 protocol), after obtaining written informed consent from each donor and approval by the
473 French Ministry of the Research (transfer agreement AC-2014-2384). Approbation by the
474 ethical department of the French Ministry of the Research for the preparation and
475 conservation of cell lines and clones starting from healthy donor human blood samples
476 has been obtained (authorization No DC-2018-3223).

477

478 ***Cell culture and stimulating conditions***

479 Total human CD8⁺ T cells were purified from healthy donor blood samples using the
480 EasySep Negative human CD8⁺ T cell isolation kit (StemCell Technologies). CD8⁺ T
481 cells were routinely ~90% pure. Memory human CD8⁺ T cells were purified from healthy
482 donor blood samples using the EasySep Human Memory CD8⁺ T cell enrichment kit
483 (StemCell Technologies), cells were routinely ~90% CD8⁺RO⁺RA⁻.

484 HLA-A2 restricted CD8⁺ T cell clones, specific for the NLVPMVATV peptide or the
485 VLAELVKQI peptide of the CMV protein pp65 were cultured in complete RPMI/HS
486 medium (RPMI 1640 medium supplemented with 5% human AB serum; Inst.

487 Biotechnologies J. Boy, Reims), minimum essential amino acids, HEPES, sodium
488 pyruvate (Invitrogen), 2-mercaptoethanol (5 μ M, Gibco) and 150 IU/ml human rIL-2 and
489 50ng/ml rIL-15). Clones were re-stimulated every 2-3 weeks in 24-wells plate with
490 1×10^6 irradiated (35 Gy) allogeneic peripheral blood mononuclear cells (isolated on
491 Ficoll Paque Gradient from fresh heparinized blood samples of healthy donors, obtained
492 from EFS) and 1×10^5 irradiated EBV-transformed B cells. Complete RPMI/HS-Medium
493 was supplemented with 1 μ g/ml PHA.

494 EBV-transformed B cells (JY) HLA-A2+ were used as target cells and cultured in RPMI
495 1640 GlutaMAX supplemented with 10% FCS and 50 μ M 2-mercaptoethanol, 10 mM
496 HEPES, 1X MEM non-essential amino acids, 1X sodium pyruvate, 10 μ g/mL
497 ciprofloxacin. Profiling of JY cells has been done using STR.

498 All cell lines are routinely screened for mycoplasma contamination using MycoAlert
499 mycoplasma detection kit (Lonza, Basel, SW).

500 For imaging flow cytometry (ImageStream®X, Merk) and confocal laser-scanning
501 microscopy human CD8⁺ T cells or CD8⁺ T cell clones were stimulated for 72h with
502 immobilized anti-CD3 (1 μ g/ml, TR66, (Valitutti, 1995)), anti-CD28 (1 μ g/ml, clone
503 CD28.2, eBioscience) and immobilized recombinant ICAM1-Fc fusion protein
504 (0.5 μ g/ml, R&D Systems) in complete RPMI/HS medium. For confocal laser-scanning,
505 cells were plated on anti-CD3/CD28/ICAM1 coated Nunc Lab-Tek Chamber Slide™
506 system 8 wells at 500 000 cells / well. For image stream analysis, cells were plated on
507 anti-CD3/CD28/ICAM1 coated 24 well plates at 1.5×10^6 cells / well.

508

509 *Image Stream analysis*

510 Staining and acquisition strategy. Cells were first stained with CellTraceTM Violet Cell
511 Proliferation Kit (CTV) in PBS (5 μ M, 20 min, 37°C). After 72 hours of stimulation (cf:
512 Cell culture and stimulating condition), cells were fixed in 1% PFA (10 min, 37°C) and
513 permeabilized in permeabilization buffer (PBS 3% BSA, 0.1% saponin, Sigma) for 5
514 min. Cells were incubated for 45 min with the indicated antibodies: AlexaFluor[®] 647
515 anti-human CD107a antibody (diluted at 1/100, clone H4A3; BD PharmingenTM), anti-
516 human Perforin (10 μ g/ml, clone δ G9; BD PharmingenTM), AlexaFluor[®] 647 anti-human
517 Granzyme B antibody (10 μ g/ml, clone GB11, BD PharmingenTM), anti-human T-bet
518 (Tbx21) (10 μ g/ml, clone 4B10; Abcam), anti-human C-myc (10 μ g/ml, clone 9E10;
519 Thermo scientific), anti-human α -tubulin (diluted at 1/100, rabbit polyclonal; Abcam).
520 The following secondary antibodies were used: AlexaFluor[®]488 or 647 goat anti-mouse
521 IgG1 (10 μ g/ml; Invitrogen), AlexaFluor[®]488 or 647 anti-rabbit (H+L) (10 μ g/ml;
522 Invitrogen). For image acquisition, cells were adjusted to 10.10⁶ - 20.10⁶ /mL in FACS
523 buffer (PBS, 1% FCS, 5% HEPES, 0.1% Azide) containing SYTOXTM Orange Dead Cell
524 Stain (recommended dilution, Thermo Fisher Scientific) for nuclear staining. Cells were
525 acquired using ImageStream[®]X (IsX; Amnis, Luminex) technology.

526 Telophase discrimination strategy. Amnis IDEAS software was used to analyze IsX data
527 and identify cells in telophase. As in classical cytometry data analysis, cells in G2/M
528 phase were first selected according to their DNA content (fluorescence of SYTOX
529 orange). A mask based on nuclear staining was employed (SpotCount Threshold (M03,
530 nucleus, 60)) to visualize the nuclei of cells/events in the G2/M fraction at the single cell
531 level. A second mask (Area Range (Threshold (M02, tubulin, 75), 50-5000, 0-0.5)) based
532 on the α -tubulin staining (to clearly identify the narrow intracellular bridge of highly

533 condensed α -tubulin that participates to midbody formation) was employed to distinguish
534 telophases from anaphases or cell-doublets. Finally, the results from both masks were
535 used to manually verify that selected cells were cells unambiguously in telophase.

536 *Analysis of cell protein distribution during telophase using Fiji.* Staining intensities of α -
537 tubulin, CTV and of the different markers of interest were analyzed on Fiji to determine
538 the percentage of proteins inherited by the two nascent daughter cells in telophase.

539 Watershed function of Fiji software was used on the α -tubulin staining intensity to
540 determine the specific areas corresponding to the two nascent daughter cells in telophase.

541 The obtained areas were converted to masks that were next applied to measure CTV and
542 the fluorescence of the different markers of interest. This procedure allowed us to
543 determine the intensity of fluorescence in the two nascent daughter cells in telophase
544 respectively. The percentage of staining in each nascent daughter cell was determined as:

545
$$\text{Fluorescence Intensity of daughter cell 1} / (\text{Fluorescence Intensity of daughter cell 1} +$$

546
$$\text{Fluorescence Intensity of daughter cell 2}) \times 100.$$
 To test the specificity of the staining
547 with the different antibodies used to study molecular repartition in telophase, we
548 measured the fluorescent intensity of secondary antibodies or isotype controls as
549 compared to specific antibodies. This analysis gave the following values of MFI: CD107a
550 70.527 isotype control 13.621; perforin 716.312, secondary mouse antibody 56.383;
551 GrzB 677.445 isotype control 13.621; T-Bet 356.228 secondary mouse antibody 56.383;
552 c-Myc 1.434.537 secondary rabbit antibody 14.231.

553

554 ***3D laser scanning microscopy on fixed cells***

555 After 72 hours of stimulation, cells were fixed in 1% PFA (10 min, 37°C).

556 Permeabilization and staining with antibodies were performed in PBS 3% BSA, 0.1%
557 saponin (Sigma) for 5 min and 45 min respectively. The following antibodies were used:
558 anti-human CD107a (10µg/ml, cloneH4A3, BD Pharmingen™) followed by
559 AlexaFluor®488 goat anti-mouse IgG1 (10µg/ml; Invitrogen), anti-human α-tubulin
560 (diluted at 1/100, rabbit polyclonal; Abcam) followed by AlexaFluor®555 goat anti-rabbit
561 (10µg/ml; Invitrogen). Nuclei were labeled with DAPI (1µg/ml, 5 min). The samples
562 were mounted in 90% glycerol-PBS containing 2.5% DABCO (Sigma) and examined
563 using a LSM710 (Zeiss) confocal microscope with a ×63 plan-Apochromat objective (1.4
564 oil) with an electronic zoom of 4. Cells in telophase were identified on the basis of
565 nuclear and tubulin marker staining. 3D images (using the z-stack function) were
566 acquired for every cell identified as being in telophase. CD107a fluorescence intensity in
567 the two nascent daughter cells was measured on 2-D image projections obtained applying
568 the Sum function of Fiji Software to z-stack series. Since the background noise made the
569 watershed function unsuitable to use, a region of interest (ROI) corresponding to the
570 nascent daughter cell was manually drawn on the basis of brightfield and tubulin staining.
571 We determined the percentage of CD107a staining in each nascent daughter cell as:
572 $\text{CD107a intensity of daughter cell 1} / (\text{CD107a intensity of daughter cell 1} + \text{CD107a}$
573 $\text{intensity of daughter cell 2}) \times 100$.

574

575 *Stimulated Emission Depletion Microscopy*

576 CTL were seeded on poly-L-lysine coated high performance coverslips and fixed in 3%
577 PFA (10 min, 37°C). Permeabilization and staining were performed in PBS 3% BSA,
578 0.1% saponin (Sigma) for 5 min and 60 min respectively. Cells were stained with an anti-

579 human Granzyme B antibody (10µg/ml, clone GB11, Thermo Scientific) followed by a
580 goat anti-mouse IgG Abberior Star 580 (Abberior Instruments). Coverslips (high
581 performance D=0.17mm +/-0.005, ZEISS, Germany) were mounted on microscopy slides
582 using Mowiol-DABCO.

583 STED images were acquired with a Leica SP8 STED 3X microscope (Leica
584 Microsystems, Germany) using a HC PL APO CS2 100X/1.4 oil immersion objective. To
585 optimize resolution without bleaching in 3-D, the 775 nm STED lasers line was applied
586 at the lowest power that can provide sufficient improvement in resolution compared to
587 confocal. Z-stack series were acquired sequentially with the pulsed 532 nm laser. For
588 image acquisition, we used the following parameters: 3 time average/line, 400 Hz scan
589 speed. STED images were subsequently deconvoluted with Huygens Professional (SVI,
590 USA) using the CMLE algorithm, with a signal to noise ratio (SNR) of 7. 3-D image
591 visualization was performed using the Fiji software.

592

593 *Live cell imaging*

594 For 3D live cell imaging, the T7 GZMB sequence was obtained by PCR amplification as
595 a XhoI-EcoRI fragment from pCMV-SPORT6-GZMB by using XhoI-T7-GZB forward
596 primer and EcoRI-GRZB noSTOP reverse primer (Employed primers: Name: XhoI-T7-
597 GzB F

598 caaCTCGAGTAATACGACTCACTATAGGGAGACCCGGTACCatgcaaccaatcctgcttctgcc

599 Name: EcoRI-GzB-noSTOP-R caaGAATTCcggcgtggcgtttcatggtttctttatccag).

600 XhoI-EcoRI fragment was cloned as a mCherry-SEpHlurin fusion construct in the
601 pmCherry-SEpHlurin vector to produce the vector pGZMB-mCherry-SEpHlurin

602 available to *in vitro* T7 transcription. The plasmid pCMV-SPORT6-GZMB and
603 pmCherry-SEpHluorin were purchased from Addgene.

604 For efficient transfection of human CTL with tagged molecules allowing to monitor lytic
605 granule repartition during mitosis, we synthesized capped and tailed poly(A) mCherry-
606 tagged Granzyme B mRNA by *in vitro* transcription from the plasmid pGZMB-mCherry-
607 SEpHluorin. One microgramme of pGZMB-mCherry-SEpHluorin was first linearized by
608 NotI digestion to be used as templates for *in vitro* transcription by the T7 RNA
609 polymerase using mMESSAGE mMACHINE T7 Ultra kit as per manufacturer's
610 protocol.

611 Human CTL were transfected using a GenePulser Xcell electroporation system (BioRad).
612 1×10^6 CTL (5days after restimulation therefore in expansion phase) were washed and
613 resuspended in 100 μ l Opti-MEM medium (Gibco) at RT with 2 μ g mCherry-tagged
614 Granzyme B mRNA (*square wave* electrical pulse at 300V, 2ms, 1 pulse). 18 hours
615 after transfection the transfection efficacy was verified by FACS analysis (typically 50-
616 80%). Transfected CTL were seeded into poly-D-lysine-coated eight-well chambered
617 slides (Ibidi, Munich, Germany) before imaging. Chambered slides were mounted on a
618 heated stage within a temperature-controlled chamber maintained at 37°C and constant
619 CO₂ concentrations (5%) and inspected by time-lapse laser scanning confocal microscopy
620 (LSM880, Zeiss, Germany with 1 image /30 seconds) for additional 5-6 hours using a
621 Tile Scan mode to enlarge the acquisition fields and capture the rare cells undergoing
622 spontaneous division during the time of acquisition.

623

624 For 4D live cell imaging, 72 hours after stimulation, CD8⁺ T cells were stained with
625 Hoechst (200 ng/ml, ThermoFisher Scientific) to sort cells in G2/M phase by flow-
626 cytometry (BD FACSAria SORP, BD Biosciences). Sorted cells were stained with
627 LysoTracker Red (200 nM ThermoFisher) for 30 min at 37°C and washed. 20 000 cells
628 in 5% HS/IL2/IL15 complete RPMI medium supplemented with 10 mM HEPES were
629 seeded into poly-D-lysine-coated eight-well chambered slides (Ibidi, Munich, Germany)
630 pre-coated with PDMS micromesh_arrays (Microsurfaces, Melburn, Australia) containing
631 100-µm-diameter wells. Cells were 4D imaged (time and z-stack) on a heated stage
632 within a temperature-controlled chamber maintained at 37°C and constant CO₂
633 concentrations (5%) and inspected over night by time-lapse laser scanning confocal
634 microscopy with a Plan-Apochromat 40x/1.3 Oil DIC M27 using an LSM780 or
635 LSM880, Zeiss, Germany) or by spinning disk time-lapse microscopy using a spinning-
636 disk microscope (Nikon) running on Metamorph software. A camera emCCD Evolve
637 (Photometrics) was used for acquisitions. Image analysis was performed using Fiji
638 software and 4-D videos and snapshots were generated with Imaris software.

639

640 *Cytotoxicity assay*

641 CTL were incubated with 200nM LysoTracker Blue[®] a probe staining the acidic lytic
642 compartment of these cells (Faroudi et al., 2003) for 30 minutes at 37°C/5% CO₂ in 5%
643 FCS/RPMI/HEPES. After washing, cells expressing the highest and lowest 5-10 %
644 LysoTracker Blue staining were sorted using a FACSARIA-SORP (BD Biosciences).
645 CTL were used for standard over-night killing assays on the day of cell. Target cells were
646 left unpulsed or pulsed with 10µM antigenic peptide during 2 hours at 37°C/5% CO₂,

647 washed three times and subsequently transferred to a 96 well U-bottom plate at
648 10×10^3 cells/100 μ l RPMI, 5% FCS/HEPES. CTL were added to the target cells at the
649 indicated effector (CTL): target (JY) ratio, in 100 μ l RPMI, 5% FCS/HEPES. Cells were
650 pelleted for 1 min at 455 g and incubated at 37°C/5% CO₂ overnight. Before FACS
651 analysis, 0.25 μ g 7-Aminoactinomycin D (7-AAD; BD Biosciences) and FITC conjugated
652 anti-CD8 antibody were added to each sample in order to measure the percentage of dead
653 target cells. For the CD107a exposure and CD8 internalization assay, sorted CTL were
654 incubated with target cells at 0.5:1 E/T ratio for 4 hours. Cells were stained with PE-cy7
655 conjugated anti-CD107a antibody and FITC conjugated anti-CD8 antibody for 30 min in
656 FACS-buffer (1% human serum, 1% Foetal Calf Serum in PBS), washed, acquired on a
657 Fortessa flow cytometer (BD Biosciences) and analysed by using FlowJo software
658 (TreeStar).

659

660 ***Statistical methods***

661 *Paired Student's t-test*, was performed to determine the statistical significance of
662 differences between the groups (GraphPad Prism software version 5).

663 *Chi-square of independence test* was performed to determine the independence between
664 the level of expression of a given marker and the capacity of a cell in telophase to
665 asymmetrically distribute this marker (Python software version 3.5).

666 *Kolmogorov-Smirnov goodness of fit test* was performed to compare law between
667 probability distribution of a marker of interest in cells in G1 (Python software version
668 3.5).

669 *Chi-square of homogeneity test* was performed (in addition Kolmogorov-Smirnov
 670 goodness of fit test) to determine where the probability distribution of a marker of interest
 671 varies (Python software version 3.5).

672

673 ***Statistical procedures***

Independence Chi2 test between heterogeneous cells and all cells	Test statistic (χ^2)	$\chi^2_{1-\alpha,dl}$	p-value (p)	Degree of freedom (dl)
CD107a, Experiment 1, 0 division	4,060439	11.07	0.540748	5
CD107a, Experiment 1, 1 division	3.565087	11.07	0.613563	5
CD107a, Experiment 1, 2 divisions	1.614763	7.815	0.656047	3
CD107a, Experiment 2, 0 division				
CD107a, Experiment 2, 1 division	0.278928	7.815	0.963942	3
CD107a, Experiment 2, 2 divisions	0.413804	7.815	0.937376	3
CD107a, Experiment 3, 0 division	2.36867	15.51	0.967574	8
CD107a, Experiment 3, 1 division	2.092976	9.488	0.718663	4
CD107a, Experiment 3, 2 divisions	0.655225	9.488	0.956734	4

674

675 Table 1: Results of independence Chi-square test in telophase

676 In the independence Chi-square test, we compare the theoretical effective ($e_{i,j}$) to the
 677 observed effective ($n_{i,j}$). The test statistic is defined by:

$$\chi^2 = \sum_{i,j} \frac{(n_{i,j} - e_{i,j})^2}{e_{i,j}}$$

678 We compare it to $\chi^2_{1-\alpha,dl}$, the quantile of the χ^2 distribution associated to the $1 - \alpha$
 679 quantile. The quantile with $1 - \alpha = 95\%$ is the value such that $P(X < \chi^2_{0.95,dl}) = 95\%$
 680 where P stands for the probability distribution of the Chi-square statistics with the
 681 associated degree of freedom dl.

682 We reject the hypothesis of independence between division of heterogeneous cells and
 683 division of all cells in one experiment when $\chi^2 \geq \chi^2_{1-\alpha,dl}$ or when the p-value p satisfies
 684 $p < \alpha = 5\%$.

685 The red boxes represent the situations where we do not reject the hypothesis of
 686 independence of division between heterogeneous cells and all cells in one experiment.

687 We shall observe that we never reject the hypothesis of independence.

Kolmogorov-Smirnov test Experiment 1	0 division		1 division		2 divisions	
	$D_{n,m}$	p-value	$D_{n,m}$	p-value	$D_{n,m}$	p-value
0 division						
1 division	0.13148	0				
2 divisions	0.220034	0	0.116283	0		

688

Kolmogorov-Smirnov test Experiment 1	0 division		1 division		2 divisions	
	$D_{n,m}$	p-value	$D_{n,m}$	p-value	$D_{n,m}$	p-value
0 division						
1 division	0.087873	0				
2 divisions	0.0891924	0	0.04634	0.03582		
3 divisions	0.054621	0.0159	0.067702	0.001185	0.047275	0.116534

689

Kolmogorov-Smirnov test Experiment 1	0 division		1 division		2 divisions	
	$D_{n,m}$	p-value	$D_{n,m}$	p-value	$D_{n,m}$	p-value
0 division						
1 division	0.14714	0.002607				
2 divisions	0.209553	0	0.143594	0		
3 divisions	0.190642	0	0.121757	0	0.038549	0.3545

690

691 Table 2: Results of Kolmogorov-Smirnov test on G1

692 The Kolmogorov-Smirnov test consists in analyzing if two independent samples follow
 693 the same law comparing their cumulative distribution function. We denote the two
 694 samples X_1, X_2, \dots, X_n and Y_1, Y_2, \dots, Y_m . If we denote by F_n and F_m their cumulative
 695 distribution respectively, the test statistic is defined by:

$$D_{n,m} = \max_{x \in R} |F_n(x) - F_m(x)|$$

696

697 We compare it to $d_{n,m,1-\alpha}$, the quantile of the associated Kolmogorov-Smirnov
698 distribution.

699 We then reject the hypothesis of adequation between cells of one division and cells of
700 one other division in one experiment when $D_{n,m} \geq d_{n,m,1-\alpha}$ or when the p-value p
701 satisfies $p < \alpha = 5\%$.

702 The red boxes represent the situation where we do not reject the hypothesis of adequation
703 between cells in one division and cells in another division. The white box represents the
704 situation where we reject this hypothesis.

705

706 **Probability of an asymmetric repartition of lytic granules**

707 To obtain a tractable formula for the computation of the probability of an asymmetric
708 repartition of lytic granules, we use a binomial model that translates that each granule
709 possesses a probability of 0.5 to attain each of the two daughter cells. The binomial
710 model also assumes that all the granules behave independently of each other.

711 In that case, the probability of an asymmetric division for n granules is then equal to

$$p_n = 2^{-n} \sum_{k < 0.4n} \frac{n!}{k!(n-k)!} + 2^{-n} \sum_{k > 0.6n} \frac{n!}{k!(n-k)!}$$

712 To evaluate the correlation level between particles (between 0 and 1) for a given
713 probability of asymmetric repartition (outside the interval [40%-60%]), we use a Monte-
714 Carlo approach where we sampled a sequence of correlated random variables distributed
715 according to a Bernoulli distribution of parameter 0.5 since to the best of our knowledge
716 there is no explicit formula to calculate a such probability of asymmetric repartition.
717 Even with a Monte-Carlo approach, the simulation is a little bit involved: if r is the

718 correlation level and if X_i is the value of the random variable at step i , then X_{i+1} is
719 obtained by :

$$X_{i+1} = X_i Y_i + Z_i (1 - Y_i) \text{(Formula A)}$$

720 where Z_i is a Bernoulli distribution of parameter 0.5 and Y_i a Bernoulli distribution of
721 parameter r . We shall verify that when X_1, X_2, \dots, X_n are sampled according to Formula A,
722 they are Bernoulli distributed and pairwise correlated with a correlation r . Hence, we then
723 mimic the correlated division with this model and then estimate the probability of
724 asymmetric repartition with 5000 Monte-Carlo simulations for each value of r and a size
725 of $n=90$ cells. We then evaluate the desired probability for r varying in a regularly spaced
726 grid from 0 to 1 with a space equal to 0.02.

727

728 **Acknowledgements**

729 We thank Dr. Stephane Manenti for discussion and critical reading of the manuscript ;
730 Dr. Hellen Robey and Dr. Pauline Gonnord for discussion. We thank Dr. Liza Filali for
731 advice in image analysis and Dr. Juliet Foote for critical reading of the manuscript. We
732 thank the flow cytometry and imaging core facilities of the INSERM UMR 1043, CPTP
733 and of the INSERM UMR 1037, CRCT, Toulouse, France.

734

735 This work was supported by grants from the Laboratoire d'Excellence Toulouse Cancer
736 (TOUCAN) (contract ANR11-LABEX), Region Occitanie (contracts RCLE R14007BB,
737 671 34 No 12052802, and RBIO R15070BB, No 14054342), Fondation Toulouse Cancer
738 Santé (contract 2014CS044) from the Ligue Nationale contre le Cancer (Equipe labellisée

739 2018) and from Bristol-Myers Squibb (No CA184-575). R.J. was supported by the Ligue
740 Nationale contre le Cancer.

741 The funders had no role in study design, data collection and analysis, decision to publish,
742 or preparation of the manuscript.

743

744 **Competing Interests statement**

745 The authors declare no competing financial interests.

746

747 **References**

- 748 Arsenio J, Kakaradov B, Metz PJ, Kim SH, Yeo GW, Chang JT. 2014. Early specification of
749 CD8+ T lymphocyte fates during adaptive immunity revealed by single-cell gene-
750 expression analyses. *Nat Immunol* **15**:365–372. doi:10.1038/ni.2842
- 751 Arsenio J, Metz PJ, Chang JT. 2015. Asymmetric Cell Division in T Lymphocyte Fate
752 Diversification. *Trends Immunol* **36**:670–683. doi:10.1016/j.it.2015.09.004
- 753 Basiji D, O’Gorman MR. 2015. Imaging flow cytometry. *J Immunol Methods* **423**:1–2.
754 doi:10.1016/j.jim.2015.07.002
- 755 Bergeland T, Widerberg J, Bakke O, Nordeng TW. 2001. Mitotic partitioning of endosomes and
756 lysosomes. *Current Biology* **11**:644–651. doi:10.1016/S0960-9822(01)00177-4
- 757 Beuneu H, Lemaitre F, Deguine J, Moreau HD, Bouvier I, Garcia Z, Albert ML, Bousso P. 2010.
758 Visualizing the functional diversification of CD8+ T cell responses in lymph nodes.
759 *Immunity* **33**:412–23. doi:10.1016/j.immuni.2010.08.016
- 760 Buchholz VR, Flossdorf M, Hensel I, Kretschmer L, Weissbrich B, Graf P, Verschoor A,
761 Schiemann M, Hofer T, Busch DH. 2013. Disparate individual fates compose robust
762 CD8+ T cell immunity. *Science* **340**:630–5. doi:10.1126/science.1235454
- 763 Buchholz VR, Schumacher TN, Busch DH. 2016. T Cell Fate at the Single-Cell Level. *Annu Rev*
764 *Immunol* **34**:65–92. doi:10.1146/annurev-immunol-032414-112014
- 765 Carlton JG, Jones H, Eggert US. 2020. Membrane and organelle dynamics during cell division.
766 *Nat Rev Mol Cell Biol* **21**:151–166. doi:10.1038/s41580-019-0208-1
- 767 Chang JT, Ciocca ML, Kinjyo I, Palanivel VR, McClurkin CE, Dejong CS, Mooney EC, Kim JS,
768 Steinel NC, Oliaro J, Yin CC, Florea BI, Overkleeft HS, Berg LJ, Russell SM, Koretzky
769 GA, Jordan MS, Reiner SL. 2011. Asymmetric proteasome segregation as a mechanism
770 for unequal partitioning of the transcription factor T-bet during T lymphocyte division.
771 *Immunity* **34**:492–504. doi:10.1016/j.immuni.2011.03.017
- 772 Chang JT, Palanivel VR, Kinjyo I, Schambach F, Intlekofer AM, Banerjee A, Longworth SA,
773 Vinup KE, Mrass P, Oliaro J, Killeen N, Orange JS, Russell SM, Weninger W, Reiner
774 SL. 2007. Asymmetric T lymphocyte division in the initiation of adaptive immune
775 responses. *Science* **315**:1687–91. doi:10.1126/science.1139393
- 776 Chiang SCC, Wood SM, Tesi B, Akar HH, Al-Herz W, Ammann S, Belen FB, Caliskan U, Kaya
777 Z, Lehmborg K, Patiroglu T, Tokgoz H, Ünüvar A, Introne WJ, Henter J-I, Nordenskjöld
778 M, Ljunggren H-G, Meeths M, Ehl S, Krzewski K, Bryceson YT. 2017. Differences in

779 Granule Morphology yet Equally Impaired Exocytosis among Cytotoxic T Cells and NK
780 Cells from Chediak–Higashi Syndrome Patients. *Front Immunol* **8**.
781 doi:10.3389/fimmu.2017.00426

782 Clark RH, Stinchcombe JC, Day A, Blott E, Booth S, Bossi G, Hamblin T, Davies EG, Griffiths
783 GM. 2003. Adaptor protein 3–dependent microtubule-mediated movement of lytic
784 granules to the immunological synapse. *Nat Immunol* **4**:1111–1120. doi:10.1038/ni1000

785 Cobbold SP, Adams E, Howie D, Waldmann H. 2018. CD4+ T Cell Fate Decisions Are
786 Stochastic, Precede Cell Division, Depend on GITR Co-Stimulation, and Are Associated
787 With Uropodium Development. *Front Immunol* **9**:1381. doi:10.3389/fimmu.2018.01381

788 Dewey EB, Taylor DT, Johnston CA. 2015. Cell Fate Decision Making through Oriented Cell
789 Division. *J Dev Biol* **3**:129–157. doi:10.3390/jdb3040129

790 Doan M, Vorobjev I, Rees P, Filby A, Wolkenhauer O, Goldfeld AE, Lieberman J, Barteneva N,
791 Carpenter AE, Hennig H. 2018. Diagnostic Potential of Imaging Flow Cytometry. *Trends*
792 *in Biotechnology* **36**:649–652. doi:10.1016/j.tibtech.2017.12.008

793 Faroudi M, Utzny C, Salio M, Cerundolo V, Guiraud M, Muller S, Valitutti S. 2003. Lytic versus
794 stimulatory synapse in cytotoxic T lymphocyte/target cell interaction: Manifestation of a
795 dual activation threshold. *Proceedings of the National Academy of Sciences of the United*
796 *States of America* **100**:14145–14150. doi:10.1073/pnas.2334336100

797 Filby A, Perucha E, Summers H, Rees P, Chana P, Heck S, Lord GM, Davies D. 2011. An
798 imaging flow cytometric method for measuring cell division history and molecular
799 symmetry during mitosis. *Cytometry Part A* **79A**:496–506. doi:10.1002/cyto.a.21091

800 Ganesan AP, Clarke J, Wood O, Garrido-Martin EM, Chee SJ, Mellows T, Samaniego-Castruita
801 D, Singh D, Seumois G, Alzetani A, Woo E, Friedmann PS, King EV, Thomas GJ,
802 Sanchez-Elsner T, Vijayanand P, Ottensmeier CH. 2017. Tissue-resident memory
803 features are linked to the magnitude of cytotoxic T cell responses in human lung cancer.
804 *Nature Immunology* **18**:940–950. doi:10.1038/ni.3775

805 Gerlach C, Rohr JC, Perie L, van Rooij N, van Heijst JW, Velds A, Urbanus J, Naik SH, Jacobs
806 H, Beltman JB, de Boer RJ, Schumacher TN. 2013. Heterogeneous differentiation
807 patterns of individual CD8+ T cells. *Science* **340**:635–9. doi:10.1126/science.1235487

808 Girel S, Crauste F. 2019. Model-Based Assessment of the Role of Uneven Partitioning of
809 Molecular Content on Heterogeneity and Regulation of Differentiation in CD8 T-Cell
810 Immune Responses. *Frontiers in Immunology* **10**:16.

811 Guldevall K, Brandt L, Forslund E, Olofsson K, Frisk TW, Olofsson PE, Gustafsson K,
812 Manneberg O, Vanherberghen B, Brismar H, Karre K, Uhlin M, Onfelt B. 2016.
813 Microchip Screening Platform for Single Cell Assessment of NK Cell Cytotoxicity. *Front*
814 *Immunol* **7**:119. doi:10.3389/fimmu.2016.00119

815 Halle S, Keyser KA, Stahl FR, Busche A, Marquardt A, Zheng X, Galla M, Heissmeyer V, Heller
816 K, Boelter J, Wagner K, Bischoff Y, Martens R, Braun A, Werth K, Uvarovskii A,
817 Kempf H, Meyer-Hermann M, Arens R, Kremer M, Sutter G, Messerle M, Forster R.
818 2016. In Vivo Killing Capacity of Cytotoxic T Cells Is Limited and Involves Dynamic
819 Interactions and T Cell Cooperativity. *Immunity* **44**:233–45.
820 doi:10.1016/j.immuni.2016.01.010

821 Hodgkin PD, Dowling MR, Duffy KR. 2014. Why the immune system takes its chances with
822 randomness. *Nat Rev Immunol* **14**:711. doi:10.1038/nri3734-c1

823 Hritzo MK, Courneya J-P, Golding A. 2018. Imaging flow cytometry: A method for examining
824 dynamic native FOXO1 localization in human lymphocytes. *Journal of Immunological*
825 *Methods* **454**:59–70. doi:10.1016/j.jim.2018.01.001

826 Huang M, Zhang J, Chen W. 2019. FACS isolation of low percentage human antigen-specific
827 CD8+ T cells based on activation-induced CD3 and CD8 downregulation. *Journal of*
828 *Immunological Methods* **472**:35–43. doi:10.1016/j.jim.2019.06.013

829 Kaminski MM, Liedmann S, Milasta S, Green DR. 2016. Polarization and asymmetry in T cell
830 metabolism. *Semin Immunol* **28**:525–534. doi:10.1016/j.smim.2016.10.002

831 Kataoka T, Sato M, Kondo S, Nagai K. 1996. Estimation of pH and the Number of Lytic
832 Granules in a CD8⁺ CTL Clone Treated with an Inhibitor of Vacuolar Type H⁺ -
833 ATPase, Concanamycin A. *Bioscience, Biotechnology, and Biochemistry* **60**:1729–1731.
834 doi:10.1271/bbb.60.1729

835 Khazen R, Muller S, Gaudenzio N, Espinosa E, Puissegur MP, Valitutti S. 2016. Melanoma cell
836 lysosome secretory burst neutralizes the CTL-mediated cytotoxicity at the lytic synapse.
837 *Nat Commun* **7**:10823. doi:10.1038/ncomms10823

838 Knoblich JA. 2008. Mechanisms of asymmetric stem cell division. *Cell* **132**:583–97.
839 doi:10.1016/j.cell.2008.02.007

840 Koivusalo M, Welch C, Hayashi H, Scott CC, Kim M, Alexander T, Touret N, Hahn KM,
841 Grinstein S. 2010. Amiloride inhibits macropinocytosis by lowering submembranous pH
842 and preventing Rac1 and Cdc42 signaling. *J Cell Biol* **188**:547–563.
843 doi:10.1083/jcb.200908086

844 Kumar BV, Kratchmarov R, Miron M, Carpenter DJ, Senda T, Lerner H, Friedman A, Reiner SL,
845 Farber DL. 2018. Functional heterogeneity of human tissue-resident memory T cells
846 based on dye efflux capacities. *JCI Insight* **3**:e123568. doi:10.1172/jci.insight.123568

847 Lemaitre F, Moreau HD, Vedele L, Bouso P. 2013. Phenotypic CD8⁺ T cell diversification
848 occurs before, during, and after the first T cell division. *J Immunol* **191**:1578–85.
849 doi:10.4049/jimmunol.1300424

850 Newell EW, Sigal N, Bendall SC, Nolan GP, Davis MM. 2012. Cytometry by time-of-flight
851 shows combinatorial cytokine expression and virus-specific cell niches within a
852 continuum of CD8⁺ T cell phenotypes. *Immunity* **36**:142–52.
853 doi:10.1016/j.immuni.2012.01.002

854 Peters PJ, Borst J, Oorschot V, Fukuda M, Krähenbühl O, Tschopp J, Slot JW, Geuze HJ. 1991.
855 Cytotoxic T lymphocyte granules are secretory lysosomes, containing both perforin and
856 granzymes. *The Journal of Experimental Medicine* **173**:1099–1109.
857 doi:10.1084/jem.173.5.1099

858 Pham K, Sacirbegovic F, Russell SM. 2014. Polarized cells, polarized views: asymmetric cell
859 division in hematopoietic cells. *Front Immunol* **5**:26. doi:10.3389/fimmu.2014.00026

860 Pollizzi KN, Sun I-H, Patel CH, Lo Y-C, Oh M-H, Waickman AT, Tam AJ, Blosser RL, Wen J,
861 Delgoffe GM, Powell JD. 2016. Asymmetric inheritance of mTORC1 kinase activity
862 during division dictates CD8⁺ T cell differentiation. *Nat Immunol* **17**:704–711.
863 doi:10.1038/ni.3438

864 Quah BJ, Parish CR. 2012. New and improved methods for measuring lymphocyte proliferation
865 in vitro and in vivo using CFSE-like fluorescent dyes. *J Immunol Methods* **379**:1–14.
866 doi:10.1016/j.jim.2012.02.012

867 Rohr JC, Gerlach C, Kok L, Schumacher TN. 2014. Single cell behavior in T cell differentiation.
868 *Trends Immunol* **35**:170–7. doi:10.1016/j.it.2014.02.006

869 Sanghavi P, D’Souza A, Rai Ashim, Rai Arpan, Padinhatheeri R, Mallik R. 2018. Coin Tossing
870 Explains the Activity of Opposing Microtubule Motors on Phagosomes. *Current Biology*
871 **28**:1460-1466.e4. doi:10.1016/j.cub.2018.03.041

872 Schindelin J, Arganda-Carreras I, Frise E, Kaynig V, Longair M, Pietzsch T, Preibisch S, Rueden
873 C, Saalfeld S, Schmid B, Tinevez J-Y, White DJ, Hartenstein V, Eliceiri K, Tomancak P,
874 Cardona A. 2012. Fiji: an open-source platform for biological-image analysis. *Nat*
875 *Methods* **9**:676–682. doi:10.1038/nmeth.2019

876 Schumacher TN, Gerlach C, van Heijst JW. 2010. Mapping the life histories of T cells. *Nat Rev*
877 *Immunol* **10**:621–31. doi:10.1038/nri2822

878 Thauinat O, Granja AG, Barral P, Filby A, Montaner B, Collinson L, Martinez-Martin N,
879 Harwood NE, Bruckbauer A, Batista FD. 2012. Asymmetric segregation of polarized

880 antigen on B cell division shapes presentation capacity. *Science* **335**:475–9.
881 doi:10.1126/science.1214100
882 Valitutti S. 1995. Sustained signaling leading to T cell activation results from prolonged T cell
883 receptor occupancy. Role of T cell actin cytoskeleton. *Journal of Experimental Medicine*
884 **181**:577–584. doi:10.1084/jem.181.2.577
885 Vasconcelos Z, Muller S, Guipouy D, Yu W, Christophe C, Gadat S, Valitutti S, Dupre L. 2015.
886 Individual Human Cytotoxic T Lymphocytes Exhibit Intraclonal Heterogeneity during
887 Sustained Killing. *Cell Rep* **11**:1474–85. doi:10.1016/j.celrep.2015.05.002
888 Verbist KC, Guy CS, Milasta S, Liedmann S, Kaminski MM, Wang R, Green DR. 2016.
889 Metabolic maintenance of cell asymmetry following division in activated T lymphocytes.
890 *Nature* **532**:389–93. doi:10.1038/nature17442
891 Xiao Z, Mescher MF, Jameson SC. 2007. Detuning CD8 T cells: down-regulation of CD8
892 expression, tetramer binding, and response during CTL activation. *Journal of*
893 *Experimental Medicine* **204**:2667–2677. doi:10.1084/jem.20062376
894

895 **Figure Legends**

896 **Figure 1: Lytic components are asymmetrically distributed in dividing CD8⁺ T cells.**

897 (A-C) Freshly isolated polyclonal CD8⁺ T cells or (D) CTL clones were stimulated by
898 immobilized anti-CD8/anti-CD28/ICAM-1 during 72h and stained with antibodies
899 directed against the indicated markers. Cells in telophase were identified using Imaging
900 Flow Cytometry (A) Left panel: Each dot represents one nascent daughter cell. Only one
901 of the two nascent daughter cells in telophase is plotted. The percentage of staining for
902 CD107a in the presented cell (*x axis*) is plotted against the percentage of staining for total
903 cell proteins (CTV, *y axis*). Asymmetric cells were defined as cells in telophase in which
904 repartition of CD107a in the nascent daughter cells was beyond the 40-60% observed for
905 CTV repartition (n=908 from 3 independent experiments). Right panel: example of
906 asymmetric and symmetric cell distribution of CD107a, as detected by Imaging Flow
907 Cytometry. (B) Left panel: The percentage of staining for perforin in the presented
908 nascent daughter cell is plotted as in panel A. Asymmetric cells were defined as indicated
909 in panel A (n=191 from 3 independent experiments). Right panel: example of asymmetric
910 and symmetric cell distribution of perforin. (C) Left panel: The percentage of staining for
911 GrzB in the presented nascent daughter cell is plotted as in panel A. Asymmetric cells
912 were defined as indicated in panel A (n=728 from 2 independent experiments). Right
913 panel: example of asymmetric and symmetric cell distribution of GrzB. (D) Left panel:
914 The percentage of staining for CD107a is plotted as in panel A. Asymmetric cells were
915 defined as indicated in panel A (n=352 from 3 independent experiments). Right panel:
916 example of asymmetric and symmetric cell distribution of CD107a.

917 Numbers highlighted in blue in the plots indicate the % of cells exhibiting asymmetric
918 repartition of the marker of interest. Red lines indicate the global distribution of the data.
919 Red numbers indicate the slope of the linear regression curve for marker distribution. See
920 Figure S1, S2, S3 and S4.

921

922 **Figure 2: CD107a⁺ vesicles uneven segregation in telophase is confirmed by confocal**
923 **laser scanning microscopy.** Freshly isolated polyclonal CD8⁺ T cells were stimulated by
924 immobilized anti-CD8/anti-CD28/ICAM-1 during 72h and stained with antibodies
925 directed against CD107a. Cells in telophase were identified using confocal laser scanning
926 microscopy. **(A)** Analysis of CD107a repartition in dividing cells. The fold increase of
927 CD107a staining in the brighter nascent daughter cell as compared to the other nascent
928 daughter cell is shown. The dotted red line indicates the limit between symmetric and
929 asymmetric cells (1,5 fold increase, corresponding to a 60-40% variation) (n=61 from 2
930 independent experiments). Each dot represents one CD8⁺ T cell in telophase. **(B)**
931 Example of an asymmetric cell in division. Green CD107a, cyan DAPI, red Tubulin. A
932 maximum intensity projection (MIP) of a z-stack of images (left panel) and one z-section
933 (right panel) are shown. See Video 1.

934

935 **Figure 3: Fate determining transcription factors do not undergo uneven distribution**
936 **in telophase.** Freshly isolated polyclonal CD8⁺ T cells were stimulated by immobilized
937 anti-CD8/anti-CD28/ICAM-1 during 72h and stained with antibodies directed against T-
938 bet **(A)** or c-Myc **(B)**. **(A):** T-bet analysis (n=926 from 3 independent experiments). **(B):**
939 c-Myc analysis (n=703 from 3 independent experiments).

940 Numbers highlighted in blue in the plots indicate the % of cells exhibiting asymmetric
941 repartition of the marker of interest. Red lines indicate the global distribution of the data.
942 Red numbers indicate the slope of the linear regression curve for marker distribution.

943

944 **Figure 4: A polarity cue is not necessary for asymmetric repartition of lytic**
945 **machinery. (A)** Freshly isolated polyclonal CD8⁺ T cells were stimulated using
946 immobilized anti-CD8/anti-CD28/ICAM-1 (left) or with PMA/ionomycin (right) during
947 72 hours and stained with antibodies directed against CD107a. Each dot represents one
948 nascent daughter cell. Only one of the two nascent daughter cells in telophase that were
949 identified by Imaging Flow Cytometry is plotted. The percentage of staining for CD107a
950 in the presented nascent daughter cell (*x axis*) is plotted against the percentage of staining
951 for total cell proteins (CTV, *y axis*). Asymmetric cells were defined as in Figure 1. Left:
952 CD107a analysis when cells were stimulated with immobilized stimuli (n=1185 from 3
953 independent experiments). Right: CD107a analysis when cells were stimulated with
954 PMA/ionomycin (n=644 from 3 independent experiments). Numbers highlighted in blue
955 in the plots indicate the % of cells exhibiting asymmetric repartition of the marker of
956 interest. Red lines indicate the global distribution of the data. Red numbers indicate the
957 slope of the linear regression curve for CD107a distribution. **(B)** Histograms represent the
958 mean and standard deviation of the percentage of asymmetric cells in the 3 independent
959 experiments. No statistical difference was revealed by paired t-test.

960

961

962

963 **Figure 5: Asymmetric repartition of CD107a⁺ vesicles reset at each division event.**

964 **(A, B)** Freshly isolated polyclonal CD8⁺ T cells were stimulated using immobilized anti-
965 CD8/anti-CD28/ICAM-1 during 72h and stained with antibodies directed against
966 CD107a. Cells in telophase were identified by Imaging Flow Cytometry. The number of
967 divisions accomplished and the cell cycle phase were determined on the basis of CTV
968 and SYTOX nuclear staining. **(A)** Each dot represents one nascent daughter cell. Only
969 one of the two nascent daughter cells in telophase that were identified by Imaging Flow
970 Cytometry is plotted. The percentage of staining for CD107a in the presented nascent
971 daughter cell (*x axis*) is plotted against the percentage of staining for total cell proteins
972 (CTV, *y axis*). Asymmetric cells were defined as in Figure 1. Numbers highlighted in
973 blue in the plots indicate the % of cells exhibiting asymmetric repartition of the marker of
974 interest. Red lines indicate the global distribution of the data. Red numbers indicate the
975 slope of the linear regression curve for CD107a distribution. See Figure S3. **(B)**
976 Histograms represent the mean and standard deviation of the percentage of asymmetric
977 cells in 3 independent experiments. No statistical difference was revealed by paired t-test.

978 **(C, D)** Statistical analysis of cells in telophase and in G1. **(C)** Cells in telophase are
979 plotted against their CD107a FI. The different curves represent cells having undergone 0,
980 1 or 2 mitoses. Each dot indicates one cell undergoing asymmetric CD107a repartition as
981 compared to its CD107a FI. The χ^2 statistical test showed that cells undergoing uneven
982 repartition of lytic machinery in telophase were randomly distributed all over the CD107a
983 expression curves (See Materials and Methods section). **(D)** Plots show cells in G1 from
984 three different experiments. Curves represent the distribution of CD107a fluorescence
985 intensity for all cells in G1. Individual plots, marked with different colors, show cells in

986 G1 at different rounds of division. The Kolmogorov-Smirnov goodness of fit test rejected
987 the hypothesis that the CD107a expression curves follow the same distribution at the
988 different division round (See Supplementary Results). The χ^2 test showed that variability
989 was distributed all over the curves. See Figure S3.

990

991 **Figure 6: Lytic granules randomly distribute on the two sides of the cleavage furrow**
992 **(A and B)** Snapshots depict typical cells in division undergoing even **(A)** or uneven **(B)**
993 repartition of lytic granules (mCherry-tagged GrzB, red) in telophase as detected by live
994 cell imaging. Images are from Video 2 and 3 respectively. Results are from 3 independent
995 experiments. **(C and D)** Snapshots depict Imaris software reconstructions of typical cells
996 undergoing even **(C)** or uneven **(D)** repartition of LTR⁺ (red) lytic granules in division as
997 detected by 4D live cell imaging. Images are from Video 4 and 5 respectively. Results are
998 from 4 independent experiments. See Videos 4-6. **(E)** Binomial modeling for the
999 behavior of the population of n granules. The curve shows the probability of lytic granule
1000 asymmetric repartition in telophase as a function of lytic granule number. **(F)** Monte-
1001 Carlo simulation of particle correlation as a function of lytic granule number and
1002 probability of lytic granule asymmetric repartition.

1003

1004 **Figure 7: CTL expressing high level of lytic granules have better killing capability.**
1005 Clonal CTL were FACS-sorted on the basis of their LysoTracker Blue staining. **(A)**
1006 Representative FACS histograms showing LysoTracker Blue staining levels on
1007 LysoTracker^{high} and LysoTracker^{low} sorted-CTL at the indicated day **(D)** after cell
1008 sorting. Numbers indicate mean fluorescence intensity. Results are representative of 3

1009 independent experiments **(B-C)** LysoTracker^{High} and LysoTracker^{Low} CTL-mediated
1010 cytotoxicity was evaluated by FACS analysis by measuring 7-AAD uptake in target cells
1011 either pulsed or not with antigenic peptide following overnight incubation with CTL at
1012 the indicated E/T ratio. **(B)** Cytotoxicity is expressed as the % of 7-AAD⁺-pulsed target
1013 cells minus % of 7-AAD⁺-unpulsed target cells (basal). Results are from 3 independent
1014 experiments. Each dot represents results from one experiment performed in triplicate.
1015 Means +/- SEM are shown. Paired t-tests were performed and P-values are indicated. **(C)**
1016 Histograms shown are from one representative experiment. Numbers indicate the
1017 percentage of 7-AAD positive target cells. **(D)** LysoTracker^{High} and LysoTracker^{Low} CTL
1018 CD107a exposure after a 4 hours incubation with target cells pulsed or not with antigenic
1019 peptide (E/T ratio 0.5:1) was evaluated by FACS analysis. Each dot represents results
1020 from 4 independent experiments performed either in duplicate or triplicate. Means +/-
1021 SEM are shown. Paired t-tests were performed and P-values are indicated. **(E)** CD8
1022 expression in LysoTracker^{High} and LysoTracker^{Low} CTL after a 4 hours incubation with
1023 target cells pulsed with antigenic peptide (E/T ratio : 0.5:1) was evaluated by FACS
1024 analysis. Results are normalized on CD8 MFI level of LysoTracker^{High} and
1025 LysoTracker^{Low} CTL cultured in the absence of target cells. Each dot represents results
1026 from 4 independent experiments performed either in duplicate or triplicate. Means +/-
1027 SEM are shown.

1028 **Supplementary figure legends**

1029 **Figure 1-supplement 1 : Gating strategy for Imaging Flow Cytometry (IsX)**

1030 **acquisition.** Based on the brightfield illumination, all events were plotted for their aspect
1031 ratio (length/width, equal 1 for perfectly round cells) and their area. Cells in telophase
1032 were defined as those exhibiting a low aspect ratio and a big area. The region of interest
1033 (gray) included cell doublets and cells in anaphase and telophase. Based on the intensity
1034 of DNA staining (represented in linear axis) cells in G2/M were selected. We then
1035 applied a mask on the IsX image gallery (as described in material and methods section) to
1036 define the limits of the nuclei. This strategy was used to determine the number of nuclei
1037 present in each gated cell. To unambiguously identify cells in telophase we applied a
1038 mask on α -tubulin staining allowing to detect condensed microtubules in an elongated
1039 shape (as described in material and methods section). This procedure allowed us to detect
1040 the midbody (a structure characteristic of telophase formed by highly condensed α -
1041 tubulin that bridges the 2 nascent daughter cells). Cells included the described gates were
1042 finally visually inspected. All the cells recognized as in telophases on the basis of nuclear
1043 and tubulin staining were included in the analysis of the markers of interest.

1044

1045 **Figure 1-supplement 2 : Analysis and representation of the repartition of markers of**

1046 **interest in dividing cells (A)** Analysis of individual cells in telophase. All IsX generated
1047 TIFF files were analyzed using the Fiji software. For each telophase cell we used 3 TIFF
1048 image corresponding to: i) CTV staining; ii) α -tubulin staining iii) and marker of interest.
1049 To standardize analysis, we used macro programming on Fiji (described in
1050 supplementary results section). To determine a rupture zone between the 2 nascent

1051 daughter cells we applied watershed function on tubulin mask. The watershed masks
1052 were used to determine the 2 nascent daughter cells in which the fluorescence intensities
1053 of CTV and of the markers of interest were measured (yellow lines). **(B)** Example of a
1054 cell exhibiting asymmetric distribution in telophase of a marker of interest. The yellow
1055 lines highlight the nascent daughter cell exhibiting a higher content of the marker of
1056 interest.

1057

1058 **Figure 1-supplement 3 : CD8⁺ T cells are efficiently stimulated on coated anti-**
1059 **CD3/anti-CD28/ICAM1.** Freshly isolated polyclonal CD8⁺ T cells previously stained
1060 with CTV were stimulated 72 hours using immobilized anti-CD3/anti-CD28/ICAM1. **(A)**
1061 Imaging Flow Cytometry shows that stimulated cell undergo several rounds of division as
1062 shown by CTV staining dilution. **(B)** Flow cytometry shows upregulation of CD137
1063 expression in stimulated cells.

1064

1065 **Figure 1-supplement 4 : Uneven lytic granule segregation in telophase in CD8⁺**
1066 **memory T cells.** The panels show staining for CD107a and perforin in human CD8⁺
1067 memory T cells stimulated and analyzed as in **Figure 1A-B**. CD107a n=978 from 3
1068 independent experiments; perforin n=1127 from 3 independent experiments. Numbers
1069 highlighted in blue in the plots indicate the % of cells exhibiting asymmetric repartition
1070 of the marker of interest. Red lines indicate the global distribution of the data. Red
1071 numbers indicate the slope of the linear regression curve for marker distribution.

1072

1073 **Figure 6-supplement 1 : Lysotracker randomly distribute on the two sides of the**
1074 **cleavage furrow**

1075 **(A and B)** Snapshots depict Imaris software reconstructions of typical cells undergoing
1076 uneven **(A)** and even **(B)** repartition of LTR⁺ (red) lytic granules in division as detected
1077 by 4D live cell imaging. Images are from Video 6.

1078

1079 **Video legends**

1080 **Video 1: 3D visualization of CD107a repartition in a telaphasic CD8⁺ T cell** The
1081 video shows 3D reconstruction of a cell in telophase. CD107a (green), α -tubulin (red)
1082 and DAPI (cyan). The images presented in **Figure 2B** has been extracted from this video.

1083

1084 **Video 2 and 3: Visualization by time-lapse confocal laser scanning microscopy of**
1085 **cell division.** Human CTL were transfected during their expansion phase with
1086 mcherryGrzB. 18 hours after transfection, cells were inspected by time-lapse laser
1087 scanning confocal microscopy for additional 5-6 hours using a Tile Scan mode to enlarge
1088 the acquisition field and to capture rare cells undergoing spontaneous division during the
1089 time of acquisition. Video 2 shows a typical cell undergoing even repartition of GrzB⁺
1090 granules. Video 3 shows a typical cell undergoing uneven repartition of GrzB⁺ granules.
1091 Snapshots of Video 2 and 3 are shown in **Figure 6 A and B.**

1092

1093 **Video 4-6: Visualization by 4D time-lapse microscopy of cell division.** G2/M sorted
1094 CTL were loaded with Hoechst (blue) and LysoTracker Red (LTR, red) and inspected by
1095 time-lapse laser scanning confocal microscopy (video 4-5) or spinning-disk microscopy

1096 (video 6) for 12h-16h. **Video 4** shows 4D reconstruction (using Imaris software) of a
1097 typical cell undergoing even repartition of LTR⁺ granules. **Video 5** shows 4D
1098 reconstruction (using Imaris software) of a typical cell undergoing uneven repartition of
1099 LTR⁺ granules. Snapshots of Video 4 and 5 are shown in **Figure 6 C** and **D**. **Video 6**
1100 shows 4D reconstruction (using Imaris software) of one typical cell undergoing uneven
1101 repartition of LTR⁺ granules and one typical cell undergoing even repartition of LTR⁺
1102 granules. Snapshots of Video 6 are shown in **Figure 6-figure supplement 1**. Results are
1103 from 4 independent experiments.

1104

1105 **Source data files:**

1106 **Figure 1-source data 1:** CD107a, perforin and granzyme B distribution between
1107 daughter cells

1108 **Figure 2-source data 1:** fold increase of CD107a staining in the brighter nascent
1109 daughter cell as compared to the other nascent daughter cell.

1110 **Figure 3-source data 1:** T-bet and c-Myc distribution between daughter cells

1111 **Figure 4-source data 1:** CD107a distribution between daughter cells after polarized and
1112 non-polarized stimulation.

1113 **Figure 5-source data 1:** CD107a distribution between daughter cells in undivided cells ,
1114 at first division and second division.

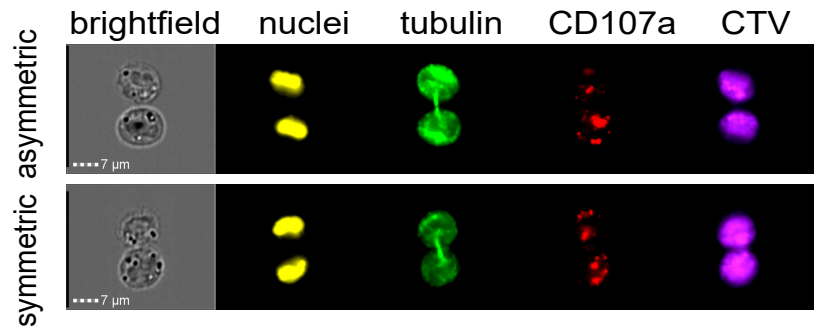
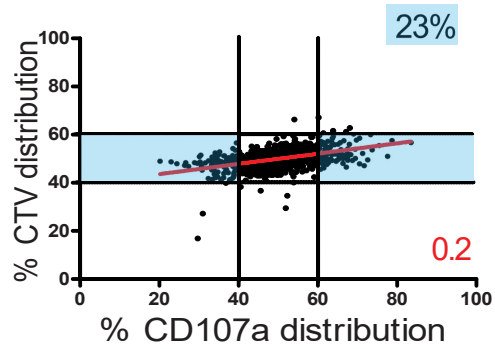
1115 **Figure 7-source data 1:** Cytotoxicity assay

1116 **Figure 7-source data 2:** CD107a Mean Fluorescence Intensity (MFI) at the surface of
1117 CD8⁺ T cells

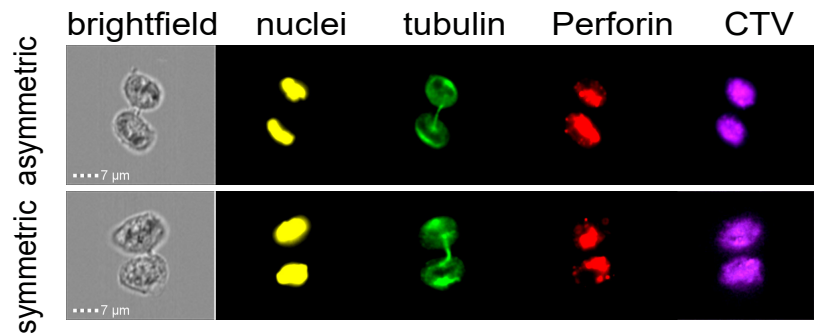
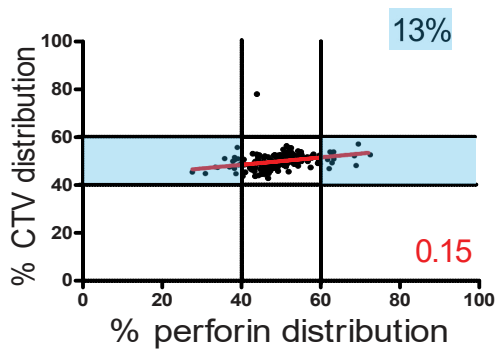
1118 **Figure 7-source data 3:** CD8 Mean Fluorescence Intensity (MFI)

Figure 1

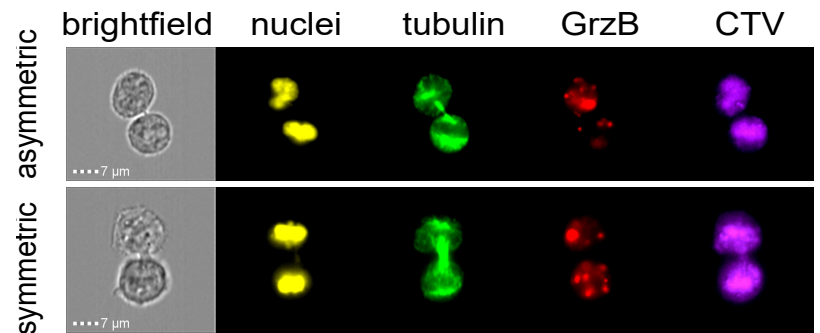
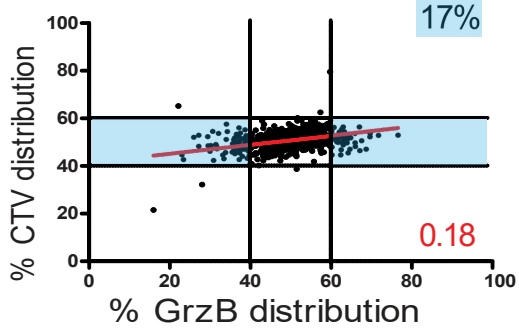
A



B



C



D

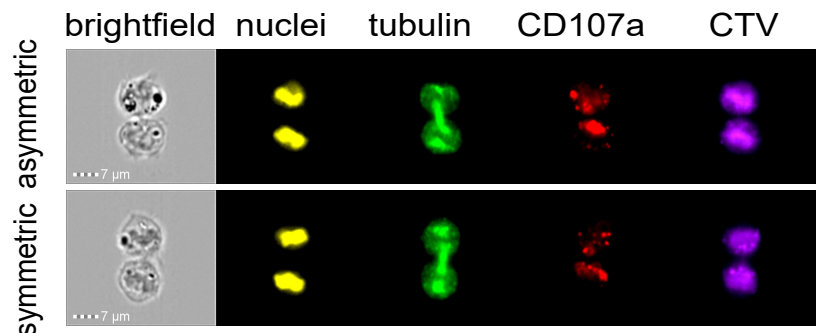
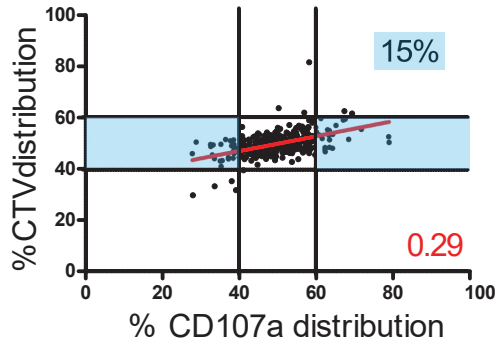


Figure 1-figure supplement 1

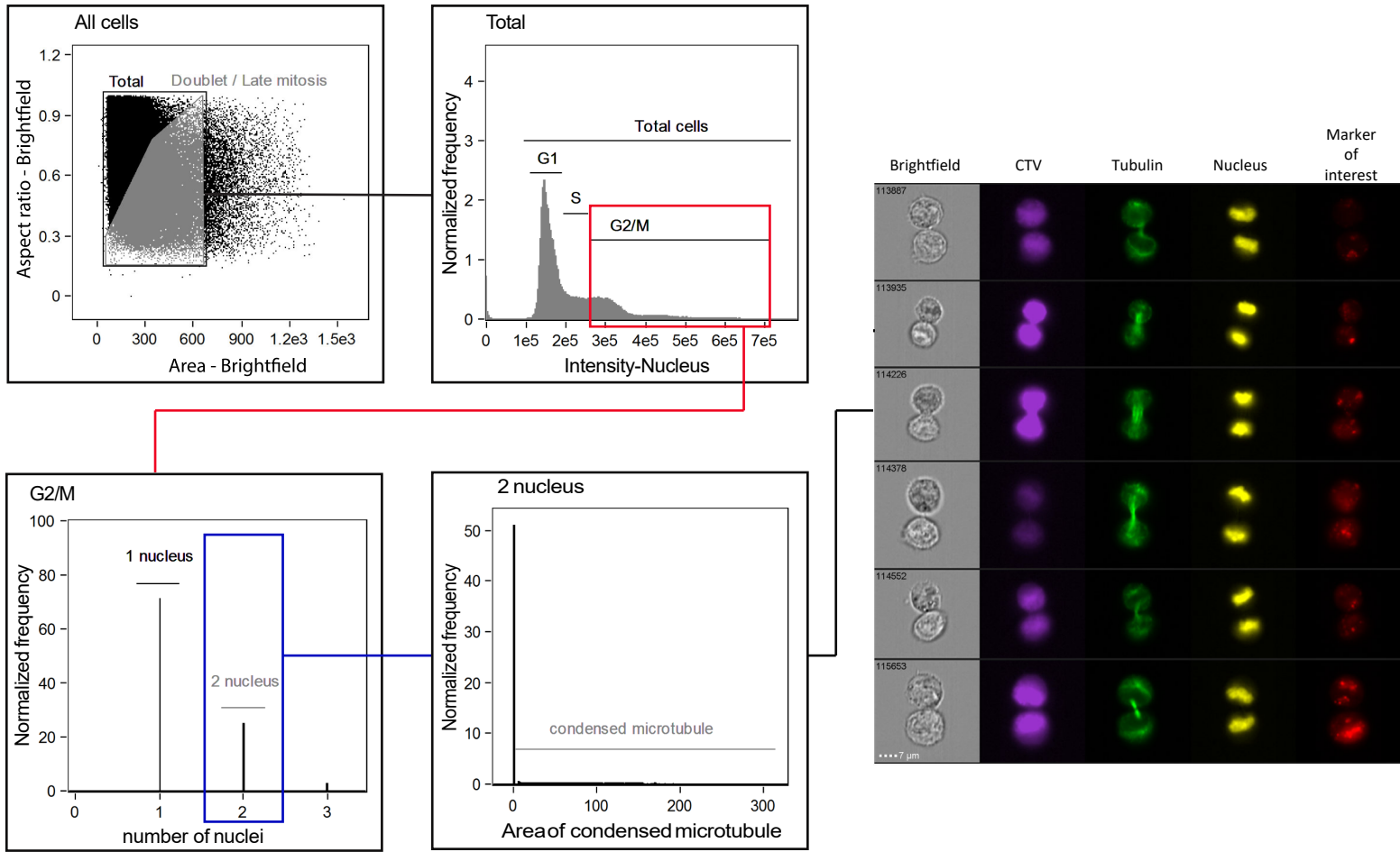
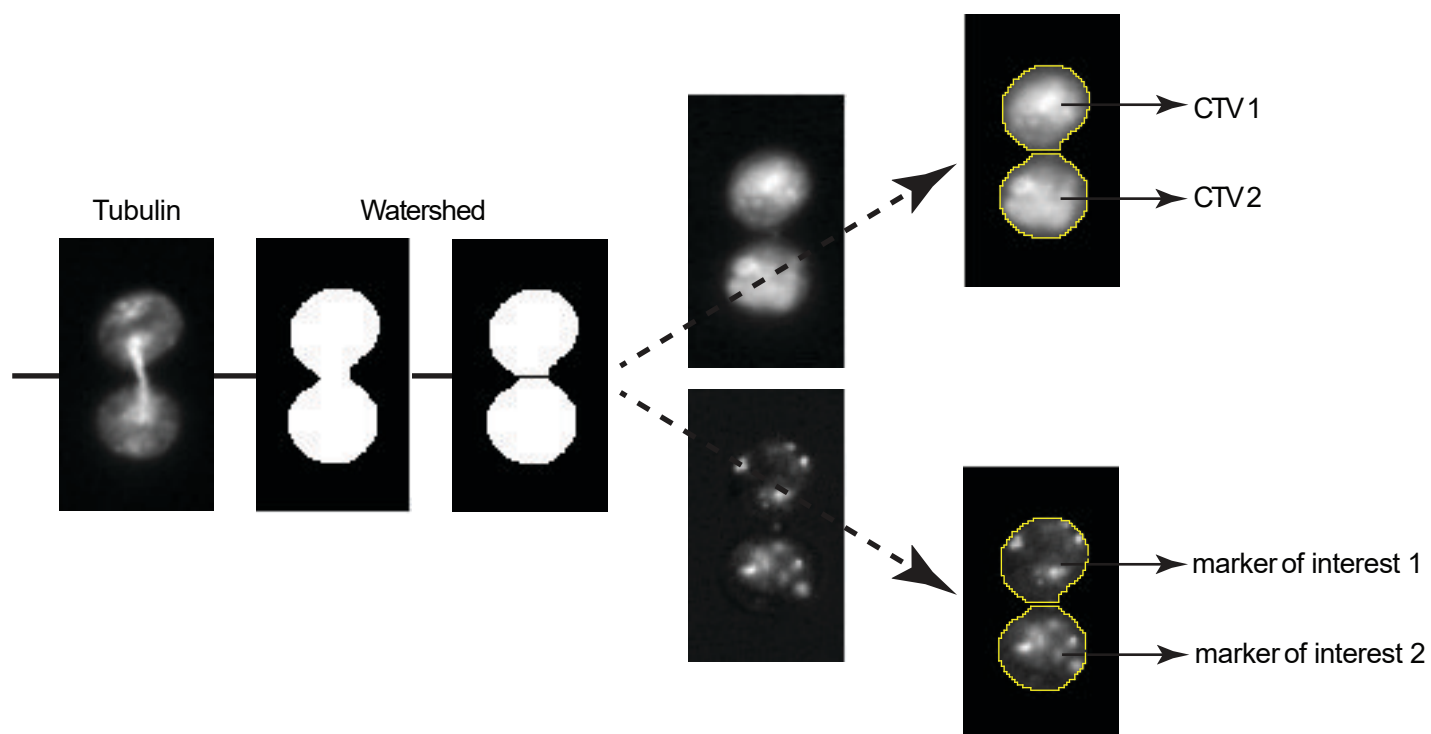


Figure 1- figure supplement 2

A



B

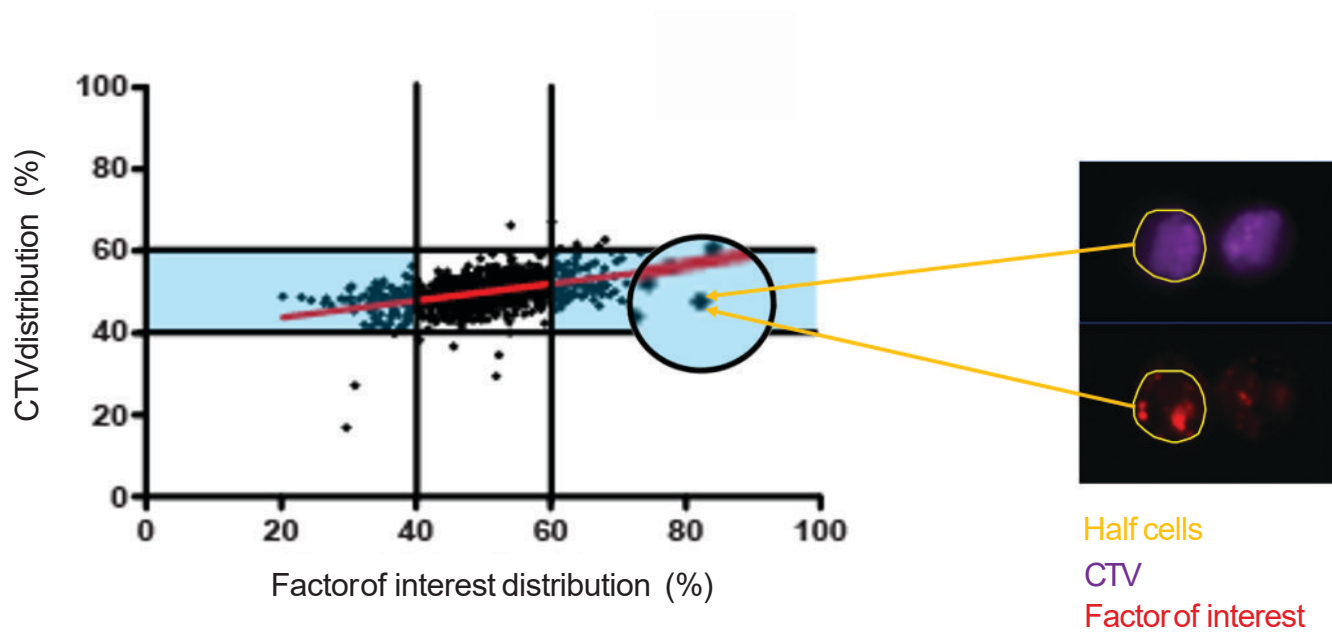
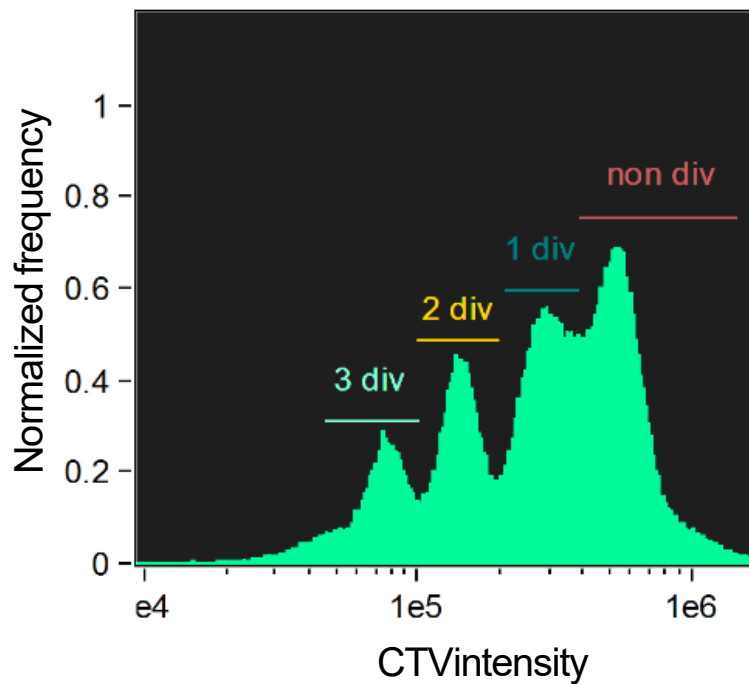


Figure 1-figure supplement 3

A



B

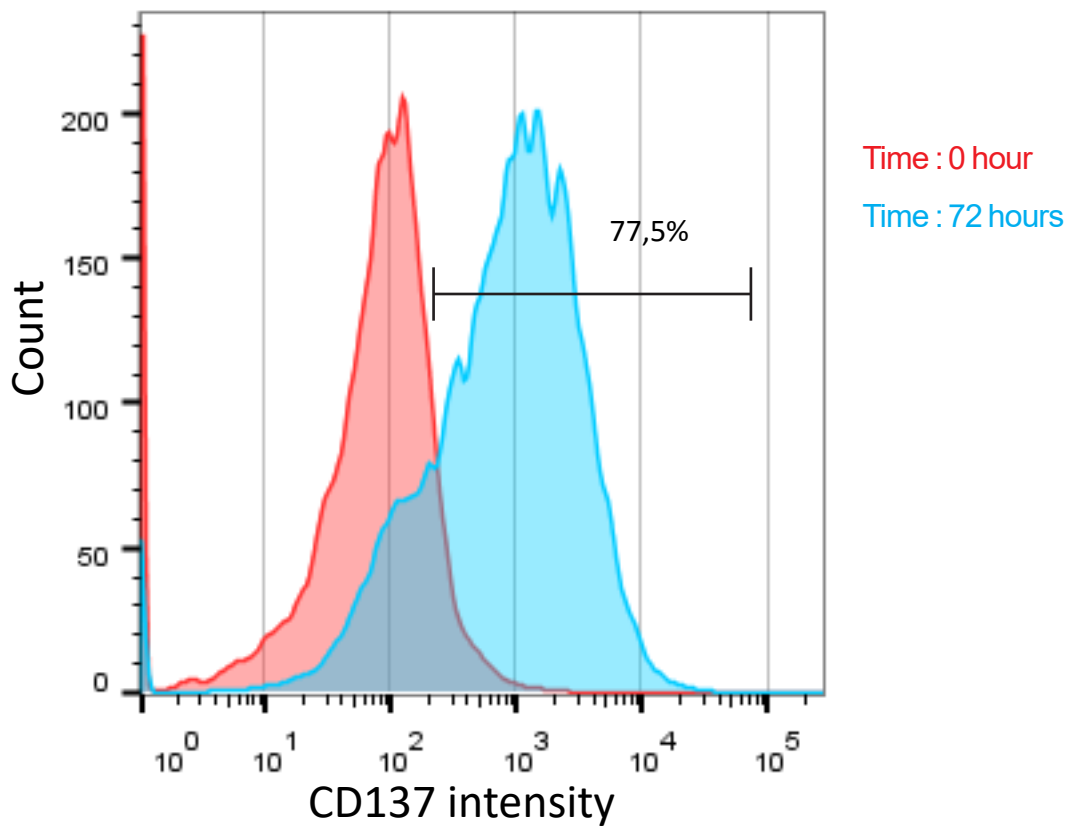


Figure 1- figure supplement 4

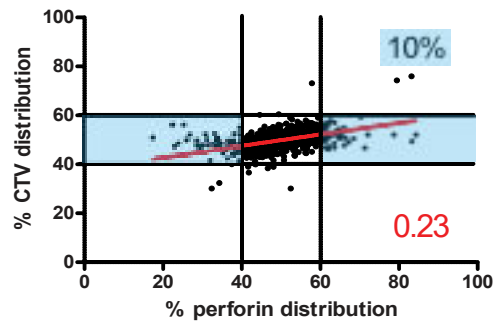
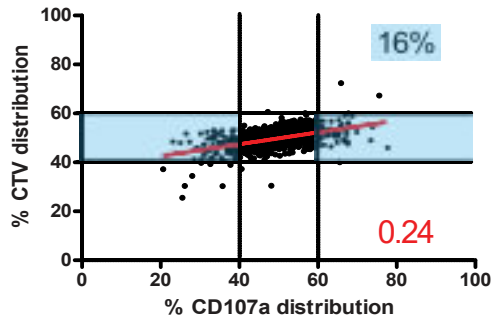


Figure 2

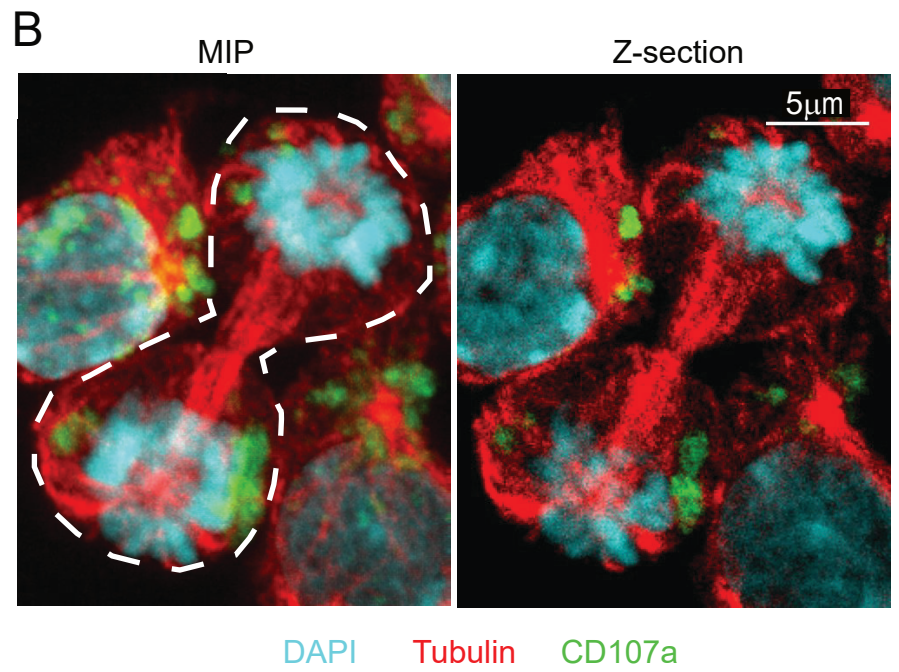
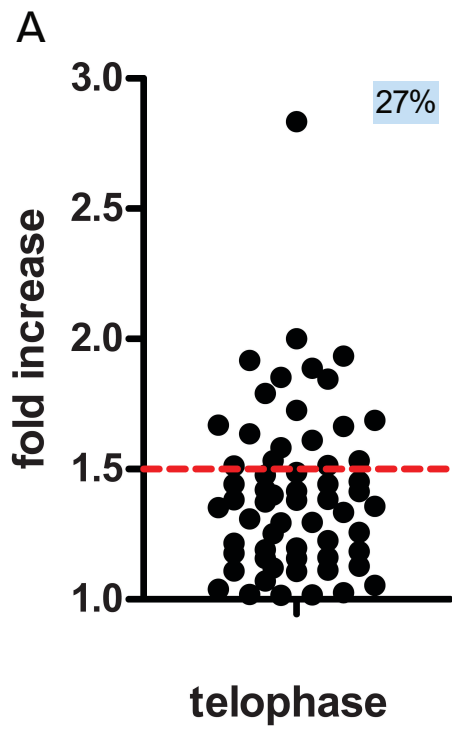


Figure 3

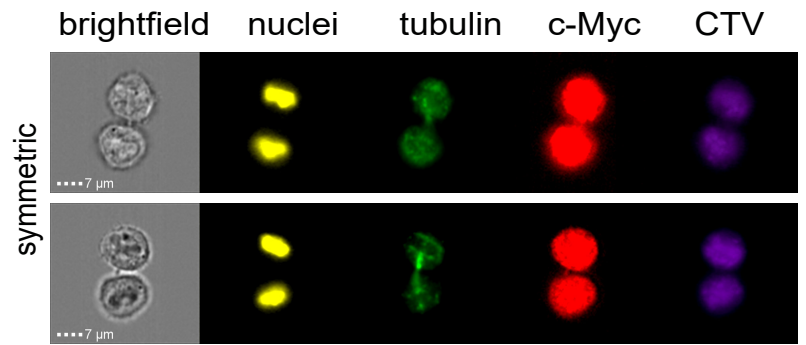
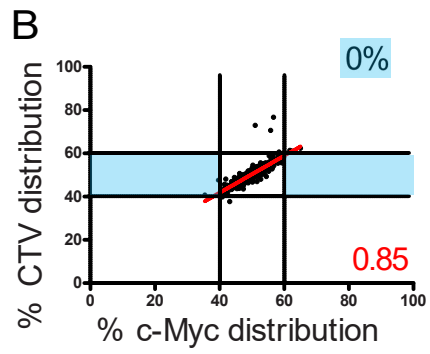
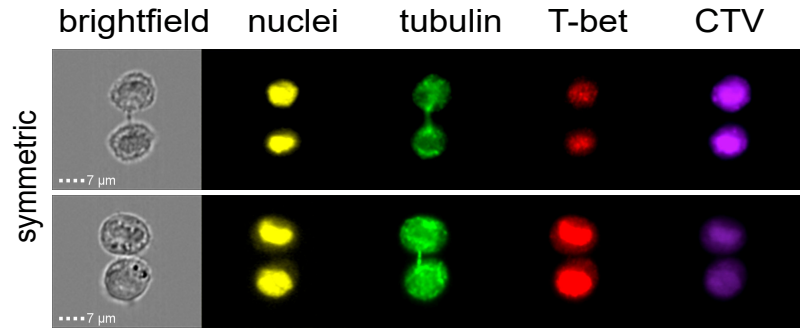
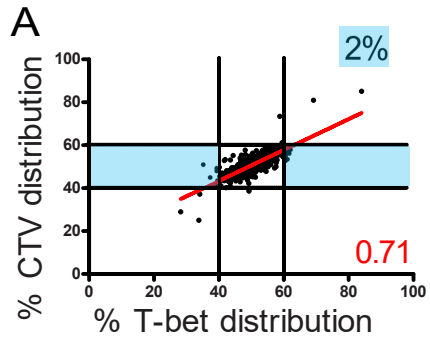
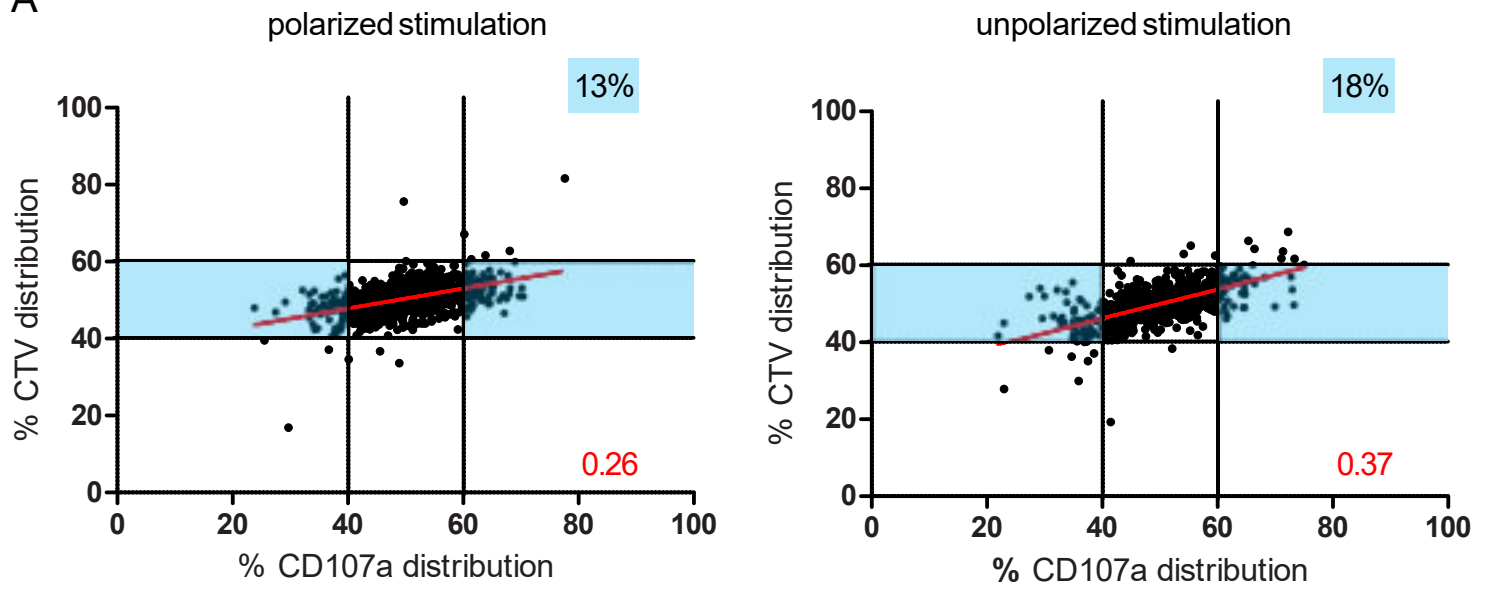


Figure 4

A



B

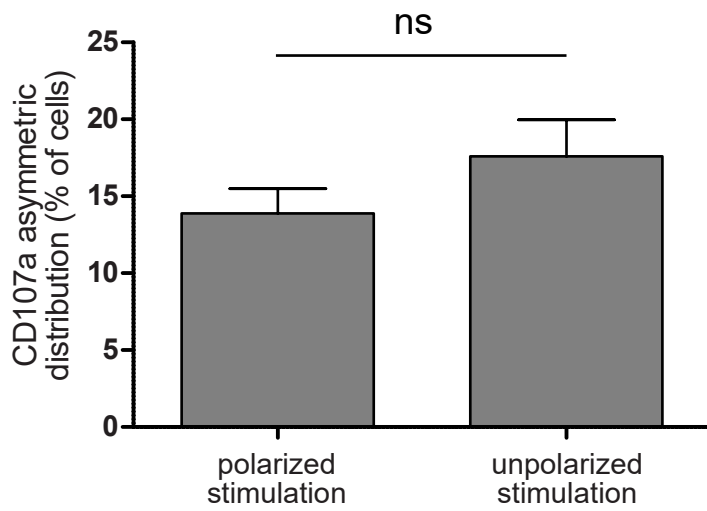
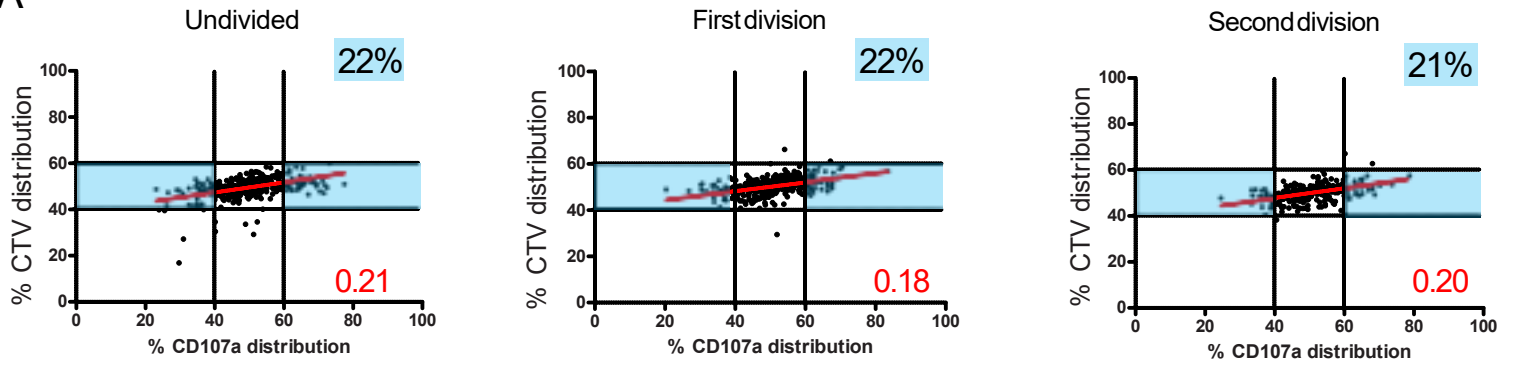
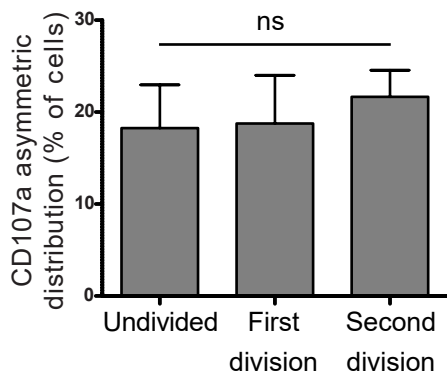


Figure 5

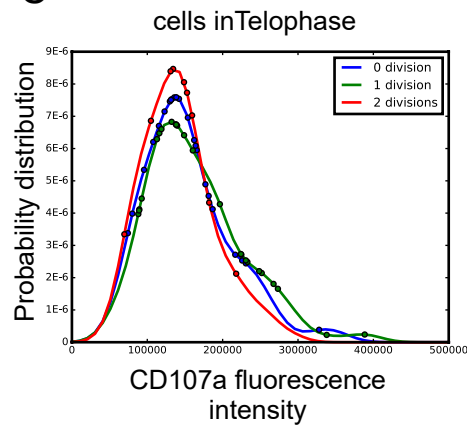
A



B



C



D

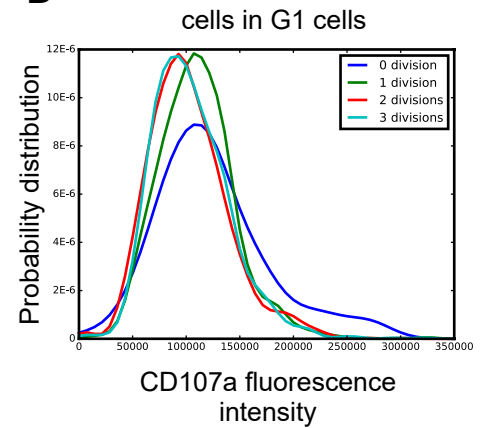


Figure 6

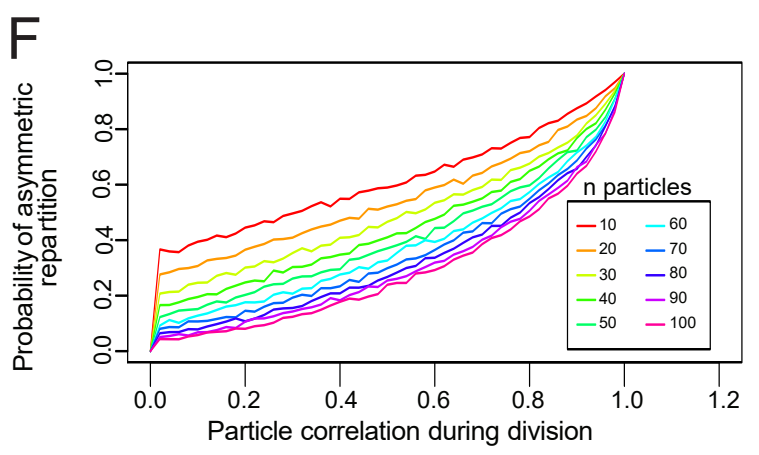
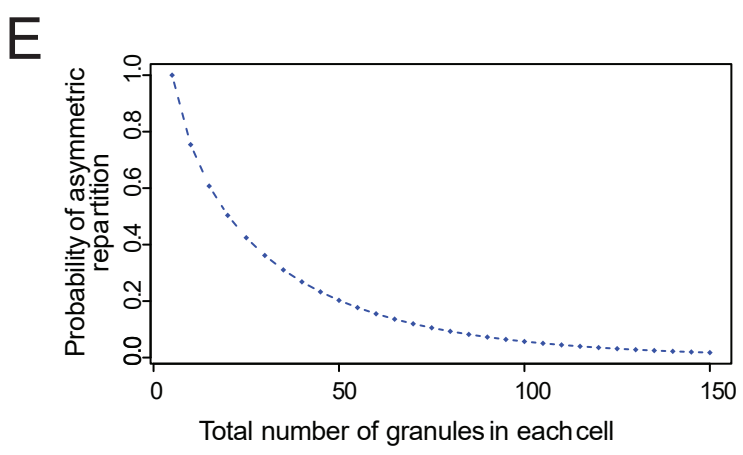
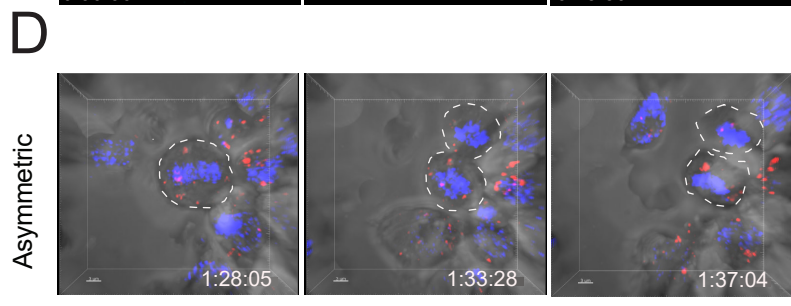
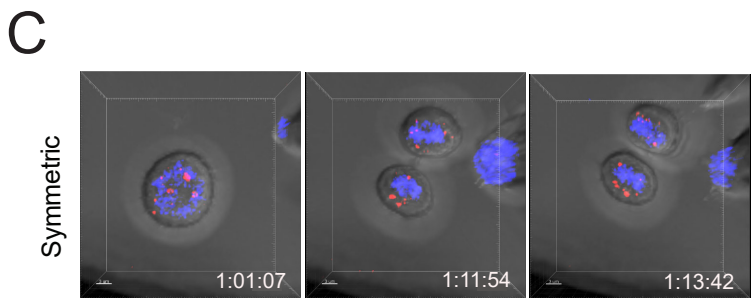
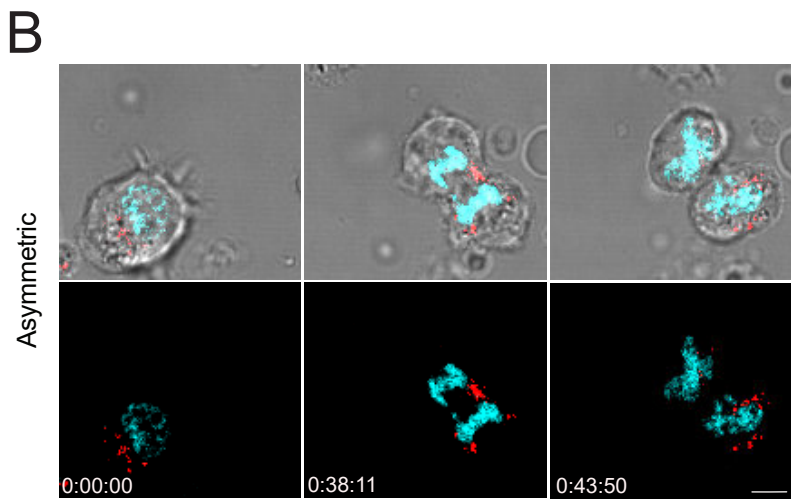
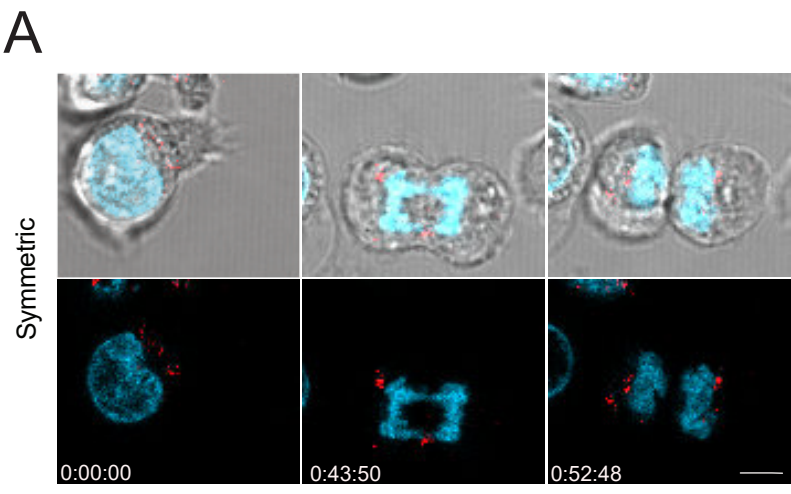
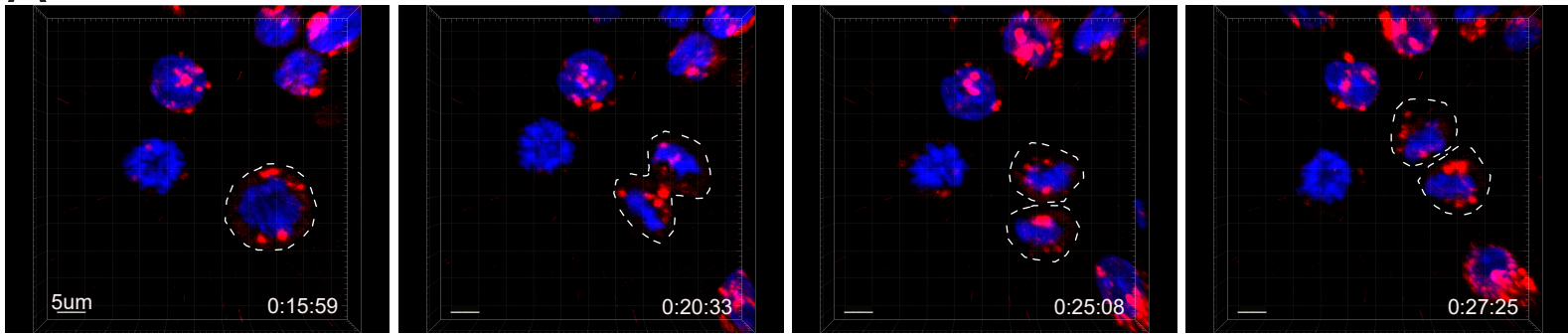


Figure 6- figure supplement 1

A



B

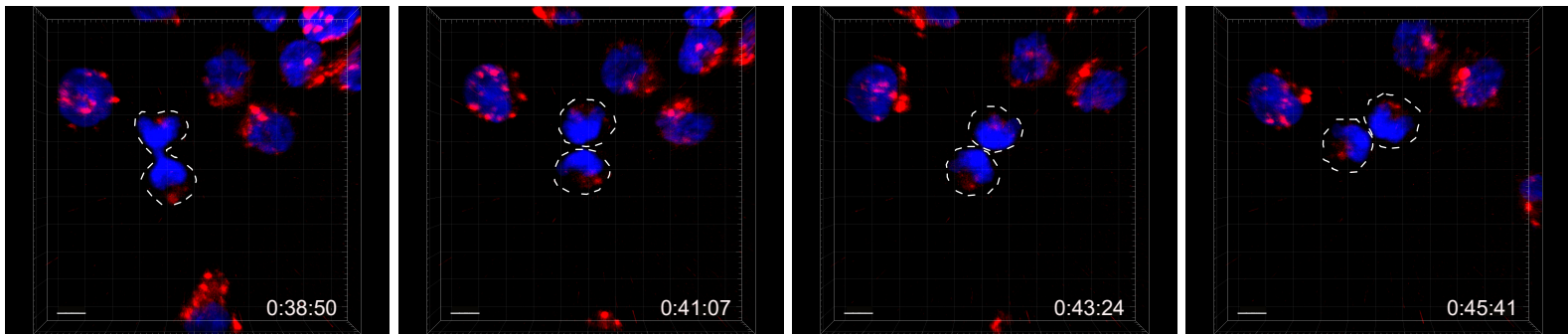


Figure 7

